Annual Review of Materials Research

Transport of Topological Semimetals

Jin Hu,[1] Su-Yang Xu,[2,3] Ni Ni,[4] and Zhiqiang Mao[5]

[1]Department of Physics and Institute for Nanoscience and Engineering, University of Arkansas, Fayetteville, Arkansas 72703, USA; email: jinhu@uark.edu

[2]Department of Physics, Massachusetts Institute of Technology, Cambridge, Massachusetts 02139, USA

[3]Laboratory for Topological Quantum Matter and Spectroscopy (B7), Department of Physics, Princeton University, Princeton, New Jersey 08544, USA

[4]Department of Physics and Astronomy and California NanoSystems Institute, University of California, Los Angeles, California 90095, USA

[5]Department of Physics, Pennsylvania State University, University Park, Pennsylvania 16802, USA; email: zim1@psu.edu

Annu. Rev. Mater. Res. 2019. 49:207–52

First published as a Review in Advance on April 10, 2019

The *Annual Review of Materials Research* is online at matsci.annualreviews.org

https://doi.org/10.1146/annurev-matsci-070218-010023

Keywords

topological semimetals, Dirac semimetals, Weyl semimetals, transport, quantum oscillation

Abstract

Three-dimensional (3D) topological semimetals represent a new class of topological matters. The study of this family of materials has been at the frontiers of condensed matter physics, and many breakthroughs have been made. Several topological semimetal phases, including Dirac semimetals (DSMs), Weyl semimetals (WSMs), nodal-line semimetals (NLSMs), and triple-point semimetals, have been theoretically predicted and experimentally demonstrated. The low-energy excitation around the Dirac/Weyl nodal points, nodal line, or triply degenerated nodal point can be viewed as emergent relativistic fermions. Experimental studies have shown that relativistic fermions can result in a rich variety of exotic transport properties, e.g., extremely large magnetoresistance, the chiral anomaly, and the intrinsic anomalous Hall effect. In this review, we first briefly introduce band structural characteristics of each topological semimetal phase, then review the current studies on quantum oscillations and exotic transport properties of various topological semimetals, and finally provide a perspective of this area.

1. INTRODUCTION

The rich cross-pollination between high-energy physics and condensed matter physics has led to deeper knowledge of important topics in physics such as spontaneous symmetry breaking, phase transitions, and renormalization (1, 2). Such knowledge has, in turn, greatly helped physicists and materials scientists to better understand magnets, superconductors, and other novel materials, leading to practical device applications (1). In the past decade, there has been significant interest in realizing high-energy particles in solid-state systems. The theoretical attempts to explain graphene's properties (3) by using solid-state physics led to an equation similar to one otherwise seen in cosmology and colliders: the Dirac equation. Following graphene's discovery, many materials with nodal band crossings, known as topological insulators and semimetals (4–11), were discovered, generating significant research excitement. The topological Dirac semimetals (DSMs) (12–14) and Weyl semimetals (WSMs) (2, 15–23) are crystalline solids whose low-energy electronic excitations resemble the Dirac (24) and Weyl (15) fermions in high-energy particle physics, respectively. In particular, although the Weyl fermion played a crucial rule in the Standard Model (15), it has never been observed as a fundamental particle. The realization of the topological WSM state (22, 23, 25–27) enables the observation of this elusive particle in physics. Topological semimetals further allow for band crossings beyond high-energy classifications. Primary examples include the type II WSMs (28) and DSMs (29), the nodal-line semimetals (NLSMs) (30), and the unconventional fermion semimetals (31–36). Due to the rich variety of crystalline and magnetic symmetry properties of condensed matter systems (37), it is likely that such breakthroughs are only the tip of an iceberg and that there are ample new topological semimetals awaiting discovery. These topological semimetals provide platforms for studying a number of important concepts in high-energy physics (e.g., the chiral anomaly) in tabletop experiments. Moreover, such materials extend the classification of topological phases from gapped matter (e.g., insulators) to gapless systems (e.g., metals).

Topological semimetals enable a kaleidoscope of novel electronic properties. They support exotic, topologically protected boundary modes such as the topological Fermi arcs and drumhead surface states. These surface states have been directly observed in spectroscopic measurements (19, 25, 27, 38–42). The Fermi arcs also lead to unusual quantum cyclotron orbits (the Weyl orbits) as observed in quantum oscillation measurements (43, 44). Because of linear dispersion and spin (pseudospin) momentum locking, low-energy electrons in topological semimetals are highly robust against crystalline disorder and imperfections, leading to very high electron mobilities (45, 46). The compensating electron and hole carriers further cause nonsaturating magnetoresistance (MR) (46–48) and magnetothermopower (49–51). The application of parallel electric and magnetic fields can break the apparent conservation of the chiral charge (10, 11, 52, 53). Such chiral anomaly leads to enhanced conductivity with an increasing magnetic field. The diverging Berry curvatures near the nodal points support distinct anomalous transport phenomena, including intrinsic anomalous Hall effects (AHEs) (54–56) and anomalous Nernst effects (57, 58). Such curvatures also support significantly enhanced optical and optoelectronic phenomena, including large (even quantized) photocurrents (59–64), second-harmonic generation (65, 66), optical activity and gyrotropy (67–69), and Kerr rotation (70, 71). Furthermore, thinning down a 3D topological semimetal into 2D may give rise to new 2D topology, including the quantum spin Hall insulator (QSHI) and the quantum anomalous Hall insulator (QAHI) (14, 20, 21, 72–76). These unconventional transport and optical properties of topological semimetals can pave the way for the realization of dissipationless electronic and spintronic devices as well as efficient photodetectors and energy harvesters.

The area of 3D topological semimetals is fast growing; many papers have been published on theoretical predictions and experimental studies. Many reviews have introduced progress in theoretical and experimental studies on topological semimetals (8–11, 76–85). In this review, we focus on electronic transport and quantum oscillation studies on topological semimetals; these two topics have not been reviewed comprehensively in previous reviews. Before we discuss these topics in detail, we first briefly introduce each prototype topological semimetal phase and discuss their band structure characteristics, topological invariants, and symmetry protections.

2. CATEGORIES OF TOPOLOGICAL SEMIMETALS

In this section, we discuss various 3D topological semimetal phases of matter, including WSMs, DSMs, NLSMs, and unconventional fermion semimetals beyond the Dirac and Weyl paradigm. For each kind of topological semimetal, we focus on three aspects: the characteristic band structure (the number of bands that cross, the dimensionality of the band crossing in k space, and the typical energy-momentum dispersion), the topological invariant and the symmetry protections, and representative materials.

2.1. Weyl Semimetals

WSMs are a class of topological semimetals that host Weyl fermions as low-energy quasiparticle excitations (2, 6–11, 15–21). In a WSM, two singly degenerate bands cross at discrete points, i.e., Weyl nodes, and disperse linearly in all three momentum space directions away from each Weyl node (**Figure 1*a***). Weyl fermions have distinct chiralities that are either left handed or right handed. The chiralities of the Weyl nodes give rise to chiral charges, which can be understood as monopoles and antimonopoles of Berry flux in momentum space. The separation of the opposite chiral charges in momentum space leads to surface Fermi arcs, whose constant energy contours are open arcs that connect the Weyl nodes of opposite chiralities on the surface.

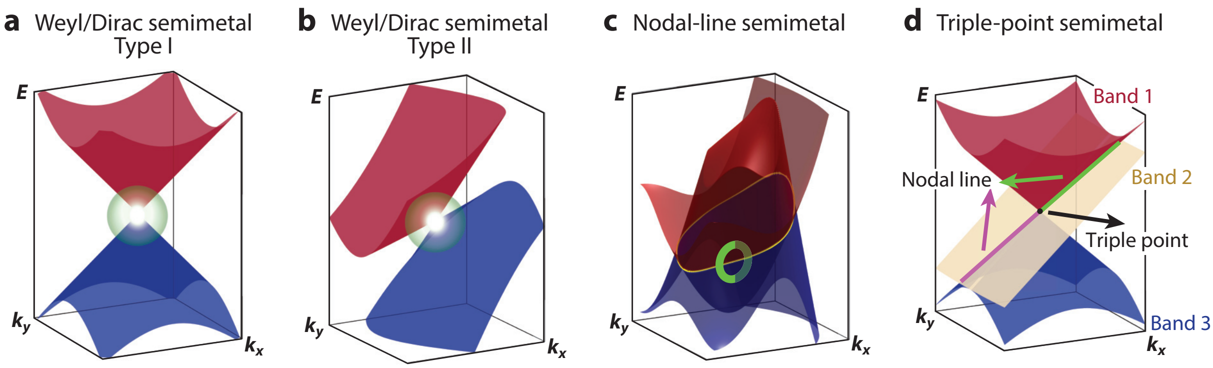

Figure 1

Schematic band structure of different types of topological semimetals. (*a*) Type I Weyl/Dirac semimetal. The degeneracy of a Weyl point is half that of a Dirac point. On a 2D closed surface (the *green spherical* surface) that encloses the Weyl node in k space, the band structure is fully gapped and therefore allows a topological invariant to be defined. Specifically, the topological invariant for a Weyl node is a chiral charge, which corresponds to the Chern number associated with the 2D closed surface. (*b*) Type II Weyl/Dirac semimetal. At the energy of the type II Weyl/Dirac node, the constant energy contour consists of an electron pocket and a hole pocket touching at the node. (*c*) Nodal-line semimetal. The conduction and valence bands are degenerate on a 1D closed loop, shown as the yellow circle in the Brillouin zone. The topological invariant of the nodal line is a winding number w, which is defined as the line integral of the Berry connection along a closed loop, shown as the green circle that interlinks the nodal line. (*d*) Triple-point semimetal. Three singly degenerate bands cross at discrete points, the triple points. The triple point can also be viewed as the meeting point between two nodal lines along the k_y axis.

Because of the existence of Weyl nodes, WSMs lack a global band gap. The absence of a global band gap prevents the definition of a topological invariant for the entire 3D bulk Brillouin zone (BZ). In contrast, on a 2D closed surface that encloses the Weyl node in k space (**Figure 1*a***), the band structure is fully gapped and therefore allows a topological invariant to be defined (19). Specifically, the Chern number associated with the 2D closed surface directly corresponds to the topological invariant of a Weyl node (i.e., the chiral charge). Mathematically, the chiral charge C can be calculated by the integral of the Berry curvature (the Berry flux) as shown below:

$$C = \int_S \mathbf{\Omega} \cdot \mathrm{d}\mathbf{S}, \tag{1}$$

where S is the 2D closed surface in k space that encloses the Weyl node and $\mathbf{\Omega}$ is the Berry curvature. Due to the chiral charge, Weyl nodes can appear at generic k points of the BZ. In the presence of translational symmetry, these Weyl nodes are topologically stable and cannot be removed without pair annihilation. The existence of Weyl nodes does not rely on any additional crystalline point group symmetries.

Real materials that host the WSM state are usually further classified into either inversion symmetry–breaking WSMs or time-reversal symmetry (TRS)-breaking WSMs. Representative inversion symmetry–breaking WSMs include the TaAs family of noncentrosymmetric crystals (22, 23, 25, 27, 39, 86–92). Representative TRS-breaking WSMs can be realized in naturally occurring ferromagnetic (FM) semimetals such as pyrochlore iridate (19), $HgCr_2Se_4$ (21), $Co_3Sn_2S_2$ (93, 94), Heuslers (95–99), and the noncollinear antiferromagnets Mn_3Sn and Mn_3Ge (57, 100–103) or by applying an external magnetic field to a nonmagnetic or antiferromagnetic (AFM) semimetal, as demonstrated in the magnetotransport experiments (104) on Na_3Bi (105), Cd_3As_2 (45, 106), $ZrTe_5$ (107), and half-Heuslers (108–110). From a different angle, WSMs can also be classified by the energy-momentum dispersions near the Weyl nodes. Type I WSMs have untilted or weakly tilted Weyl cones with a point-like Fermi surface when the chemical potential is placed at the Weyl node. By contrast, type II WSMs have strongly tilted Weyl cones (**Figure 1*b***) (28). Their Fermi surface consists of electron and hole pockets that touch at the type II Weyl nodes. Representative type II WSMs include WTe_2 (28, 111–113), $MoTe_2$ (114–122), $TaIrTe_4$ (123, 124), and $(W/Mo)P_2$ (125). These different classifications are not mutually exclusive. For instance, $MoTe_2$ is not only an inversion symmetry–breaking WSM but also a type II WSM.

2.2. Dirac Semimetals

DSMs host Dirac fermions as low-energy quasiparticle excitations (12–14, 38, 126–131). In a DSM, two doubly degenerate bands cross to form a Dirac node and disperse linearly in all three momentum directions away from the node. Each Dirac node can be viewed as a pair of degenerate Weyl nodes of opposite chiralities. Since a pair of degenerate Weyl nodes of opposite chiralities is in general unstable and may annihilate, additional crystalline point group symmetries are needed to realize a stable DSM phase (131). One route is to rely on uniaxial rotational symmetries (131). Specifically, a band inversion can create a pair of 3D Dirac nodes on the opposite sites of the time-reversal invariant momenta. Representative DSMs of this kind include Na_3Bi (13, 38, 126) and Cd_3As_2 (14, 127–130) (type I) as well as VAl_3 (29) (type II). Another route is to rely on nonsymmorphic symmetries, i.e., glide reflections and screw rotations. It has been theoretically shown that nonsymmorphic symmetries can lead to nontrivial band connectivity at the BZ boundaries, giving rise to filling-enforced DSMs or NLSMs, depending on the specific space groups (12, 132–135). Representative filling-enforced DSM candidates include β-BiO_2 (12) and distorted spinels (132). Furthermore, a DSM can be realized as the critical point of the topological phase transition between a trivial insulator and a topological insulator. This is achieved in the $BiTl(S_{1-x}Se_x)_2$ (12, 136), $Bi_{2-x}In_xSe_3$ (137), and $Pb_{1-x}Sn_xTe$ (138) systems by fine-tuning the chemical doping concentration. Alternatively, compounds like $ZrTe_5$ (107, 139, 140) and those in the $SrMnSb_2$ family (141–143) naturally sit near the critical point of such a topological phase transition and therefore approximate a DSM state. According to current theoretical understanding, Dirac nodes are not associated with any nontrivial topological invariant (i.e., they have zero chiral charge) (144).

2.3. Nodal-Line Semimetals

In NLSMs, conduction and valence bands cross at 1D lines in k space (**Figure 1*a***) (30, 40, 78, 85, 133, 134, 145–161). Compared to DSMs/WSMs, the electronic structure of NLSMs is distinct in three aspects: (*a*) The bulk Fermi surface consists of 1D lines in NLSMs but of 0D points in WSMs; (*b*) the density of states (DOS) is proportional to $(E - E_F)^2$ in NLSMs but to $|E - E_F|$ in WSMs; and (*c*) on the surface, nodal lines are accompanied by drumhead-like surface states, whereas Weyl nodes are connected by 1D Fermi arc surface states.

We now discuss the topological invariant of NLSMs. We consider a 1D closed loop that interlinks the nodal line in k space (**Figure 1*c***). The band structure is fully gapped and therefore allows for the definition of a topological invariant, i.e., the winding number (150). Mathematically, the winding number w is defined as the integral of the Berry connection along the 1D closed loop that links the nodal line as shown below:

$$w = \int_l \mathbf{A} \cdot \mathrm{d}\mathbf{l}, \qquad 2.$$

where l is the 1D closed loop that links the nodal line and $\mathbf{A}$ is the Berry connection.

NLSMs also come in a variety of forms, depending on the characteristic band structure and the symmetry protection. First, nodal lines can be closed loops (also termed nodal circles) inside the 3D BZ. Such nodal circles are naturally formed by a band inversion. The nodal circles are further classified on the basis of the symmetry protection. There are nodal circles that are strictly gapless only in the absence of spin-orbit coupling (SOC) (78, 146, 149, 150). They are usually protected by the combination of TRS and inversion symmetry (78, 146, 150). Representative materials include Cu_3N (149), Ca_3P_2 (147), Cu_3PdN (148), and those in the ZrSiS family (154–158). Alternatively, nodal circles can be formed in noncentrosymmetric crystals protected by a mirror plane. These nodal circles are stable even upon the inclusion of SOC. Representative materials include $PbTaSe_2$, $TlTaSe_2$, and CaAgAs (40, 145, 159, 160). Second, nodal lines can also be a straight line that span across the BZ. Representative materials include those in the $BaNbS_3$ family (161). Third, nodal circles can interlink with each other in k space, forming Hopf links and nodal chains (162–167). These Hopf links and nodal chains may be protected by the presence of multiple perpendicular mirror planes (167) or by nonsymmorphic symmetries (162, 163).

2.4. Unconventional Fermion Semimetals

In contrast to high-energy physics, solid-state crystals can support band crossings beyond the Dirac/Weyl paradigm (31–36). These band crossings, broadly referred as unconventional fermions, include three-, four-, six-, and eightfold degeneracies (31).

Here we take a particular type of three-band crossing as an example (33–36, 168–170). In such a triple-point semimetal, three singly degenerate bands cross at discrete points, the triple points (**Figure 1*d***). Moving away from one triple point along k_x or k_z, all three bands become nondegenerate. By contrast, moving away along k_y, bands 1 and 2 remain degenerate for $-k_y$, whereas bands 2 and 3 remain degenerate for $+k_y$. Therefore, the triple point can also be viewed as the meeting point between two nodal lines along the k_y axis. These triple points are protected by the combination of a uniaxial rotational axis, mirror planes, and TRS. These triple points are not associated with any topological invariant due to the lack of a global band gap on any 2D closed surface that encloses the triple point. Representative materials include MoC, WC, MoP, and ZrTe (33–36, 169, 170).

3. TRANSPORT SIGNATURES OF TOPOLOGICAL SEMIMETALS

The relativistic nature of the Dirac and Weyl fermions in topological semimetals manifests in many distinct transport properties, including extremely large MR, high mobility, light effective mass, nontrivial Berry phase, the chiral anomaly, and the AHE. These relativistic fermion properties have great potential for future electronic and spintronic applications. Characterization of relativistic fermions through transport measurements provides a convenient approach for verifying a nontrivial topological state, complementary to the direct observation of nontrivial band topology by ARPES experiments. In this section, we summarize these transport signatures of topological DSMs and WSMs.

3.1. Magnetoresistance

Electron transport in topological semimetals is usually strongly affected by external magnetic field. Large MR is a common signature often seen in most DSMs and WSMs. MR is usually expressed as the change in resistance (resistivity) under field normalized by the zero-field resistance (resistivity), i.e., $[R(B) - R(B = 0)]/R(B = 0)$ or $[\rho(B) - \rho(B = 0)]/\rho(B = 0)$. The transverse MR, measured with the field perpendicular to the current direction, can reach up to 0.1–1 million percent at low temperatures (0.5–5 K) and a field of 9 T (see **Table 1**), without any sign of saturation up to 30–100 T in WSMs/DSMs such as Cd_3As_2, $PtBi_2$, WTe_2, and NbP (46, 48, 171, 172). A power law field dependence (MR $\propto B^n$) is usually seen in various topological semimetals, with the exponent n ranging from 1 to 2 (45, 46, 48, 107, 171–187).

In a simple metal, a positive transverse MR with quadratic field dependence is generally expected due to the Lorentz effect (47). Such Lorentz effect–induced orbital MR is usually weak and saturates for systems with a closed Fermi surface, contrasted with the giant, nonsaturating MR seen in topological semimetals. The origin of the unusually large MR of topological semimetals has been intensively studied. Electron-hole compensation has been proposed to be a possible mechanism (46, 48, 171). However, reports also indicate that carrier compensation is not achieved in some topological semimetals (188, 189). An alternative explanation is that the backscattering at zero field is strongly suppressed by some protection mechanisms associated with nontrivial band topology but is significantly enhanced by magnetic fields (45).

The strong coupling between MR, high mobility, and linearly dispersed Dirac/Weyl cones may provide some clues for further understanding of the large MR. High mobility is another signature accompanied with large MR in topological semimetals. Mobility (μ) is related to conductivity σ via $\sigma = nq\mu$, where n and q are the carrier density and charge, respectively. For a single-band system, the Hall coefficient $R_H = 1/nq$, and thus $\mu = \sigma \cdot R_H$. However, in multiple-band systems, the field dependence of Hall resistivity ρ_{xy} deviates from linearity. **Figure 2*a*** shows one example. In this case, the Hall coefficient, defined as $d\rho_{xy}/dB$, becomes field dependent, and both mobility and carrier density cannot be directly derived as for a single-band system. A commonly used approach for analyzing the transport properties of multiband systems is the multiple-band model, i.e., assuming that the contributions of various bands to the conductivity are additive. In practice, for a system with more than two bands, a further simplified model, which considers only one electron

Table 1 Parameters obtained from transport and quantum oscillation experiments at base temperatures (1.5–5 K), including magnetoresistance (MR) at 9 T, residual resistivity ρ_{res}, transport mobility μ_T, quantum relaxation time τ_q, quantum mobility μ_q, and effective mass ratio m^*/m_0

	MR at 9 T	ρ_{res} (μΩ·cm)	μ_T [cm^2/(V·s)]	τ_q (ps)	μ_q [cm^2/(V·s)]	m^*/m_0	Reference(s)
Cd_3As_2	34.5–1,336	0.032–46.5	4×10^3–8.7×10^6	0.03–0.21	4,700–6,000	0.023–0.26	45, 172, 178, 236, 237, 272
Na_3Bi	5.69–97.1	1.72–87	5,500–78,900	0.0816	NA	0.11	105, 176
TaAs family	3–30,000	0.63–1.9	18,000–10,000,000	0.038–1.1	32,000	0.021–0.68	46, 179–183, 191–194, 225, 227, 243
WTe_2	4,000–25,000	0.39–1.9	24,000–176,000	NA	NA	0.41–0.46	48, 184, 186, 231
$MoTe_2$	2,653	28	16,000–58,000	NA	NA	0.8–2.9	337–340
$PtSn_4$	1,000–2,100	NA	NA	NA	14,257–15,809	0.05–0.36	341–343
$PtBi_2$	12,000	NA	NA	NA	NA	NA	171
$Pt(Te/Se)_2$	A few tens	NA	3,600–5,500	NA	NA	0.11–3.6	229, 344
$PdTe_2$	A few tens	NA	NA	0.18–0.65	1,293–6,209	0.04–1.16	229, 248
AMn(Sb/Bi)$_2$ (A = Ca, Sr, Ba, Yb)	1	NA	1,500–3,400	NA	NA	NA	141, 143, 173, 175, 213, 234, 235, 238, 239, 247, 283, 345, 346
WHM[a]	1.3–1,400	0.052	2,000–28,000	0.025–0.35	209–10,000	0.025–0.27, 1.32[b]	156, 222, 226, 228, 232, 233, 245, 347

NA denotes not available.

[a]MR, effective mass, and quantum relaxation time widely vary in different *WHM* materials, possibly due to the spin-orbit coupling gap, which varies with the atomic number.

[b]This result is caused by the mass enhancement at low temperatures (245).

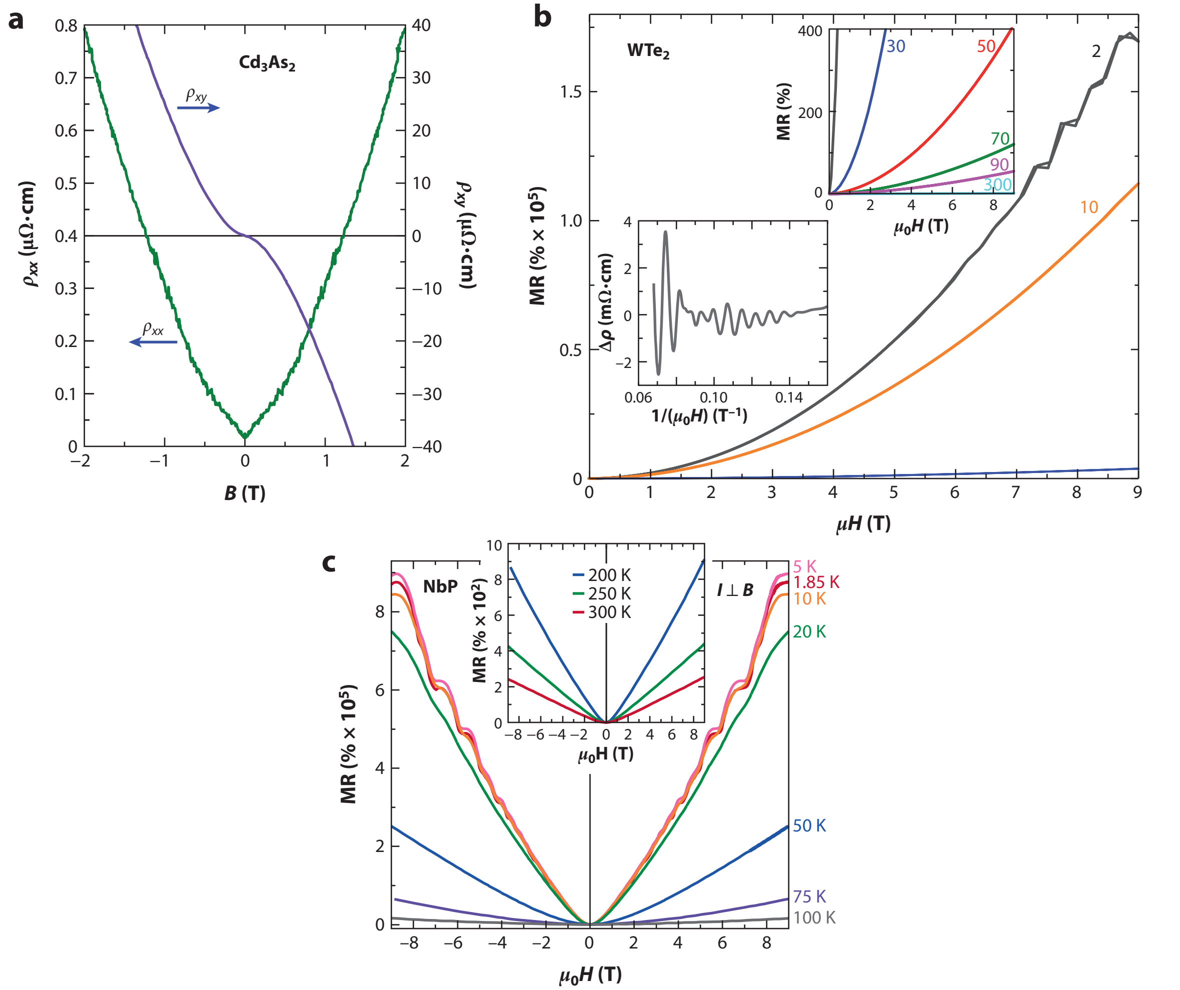

Figure 2

Magnetoresistance (MR). (*a*) Magnetic field dependence of the longitudinal (ρ_{xx}) and transverse (Hall) (ρ_{xy}) resistivity for Cd_3As_2. (*b*) MR normalized by the zero-field resistivity for WTe_2 at 2 K and 10 K. Shubnikov–de Haas (SdH) oscillation is seen for the $T = 2$ K data. (*Upper inset*) MR at higher temperatures. (*Lower inset*) Oscillatory component of the resistivity oscillation, obtained by subtracting the smooth MR background. (*c*) MR normalized by the zero-field resistivity for NbP at various temperatures. SdH oscillation is seen at $T < 10$ K. (*Inset*) MR at higher temperatures. Panels *a* and *b* adapted from References 45 and 48, respectively, with permission from Springer Customer Service Centre GmbH, copyright 2014. Panel *c* adapted from Reference 46 with permission from Springer Customer Service Centre GmbH, copyright 2015.

band and one hole band, is widely used to describe the longitudinal resistivity (ρ_{xx}) and transverse resistivity (ρ_{xy}, i.e., the Hall resistivity), as shown by Equations 3 and 4 below (190):

$$\rho_{xx} = \frac{(n_e\mu_e + n_h\mu_h) + (n_e\mu_e\mu_h^2 + n_h\mu_h\mu_e^2)B^2}{(n_e\mu_e + n_h\mu_h)^2 + \mu_e^2\mu_h^2(n_h - n_e)^2B^2} \cdot \frac{1}{e}, \qquad 3.$$

$$\rho_{xy} = \frac{(n_h\mu_h^2 - n_e\mu_e^2) + \mu_h^2\mu_e^2(n_h - n_e)B^2}{(n_e\mu_e + n_h\mu_h)^2 + \mu_h^2\mu_e^2(n_h - n_e)^2B^2} \cdot \frac{B}{e}, \qquad 4.$$

where n_e (n_h) and μ_e (μ_h) are the density and mobility of the electron (hole) band, respectively. From the simultaneous fitting for $\rho_{xx}(B)$ and $\rho_{xy}(B)$ by using such a two-band model, both the densities and mobilities of the electron bands and hole bands can be obtained. Clearly, for a real system with more than one electron or hole band, this oversimplified model averages electron and hole bands and neglects any interband interactions. Although adding more bands to the above model is possible in principle, more accurate results may not be obtained with an overparameterized model. In fact, the two-band model already yields reasonable results for a variety of material systems, so it is reasonable to extend its application to topological semimetals.

Equation 3 indicates that ρ_{xx} tends to saturate at high fields where the B^2 terms dominate. Only when $n_e = n_h$, i.e., the case of electron-hole compensation, $\rho_{xx} \propto B^2$ without saturation. Under such a circumstance, large MR is expected when mobility is high. **Table 1** shows the mobilities of some representative topological semimetals acquired from two-band model analysis; the mobilities are indeed high, in the range of 10^3–10^6 cm^2/(V·s). Such high transport mobility is consistent with the ultralow residual resistivity at the zero-temperature limit ($\sim n\Omega$ to a few $\mu\Omega$; see **Table 1**) as well as with the high quantum mobility revealed by quantum oscillation studies (discussed in Section 3.2.2).

The two-band model, while widely used, provides only an approximate description for the magnetotransport properties of multiple-band materials. First, Equations 3 and 4 are not applicable if there are open orbits, which occur when the Fermi surface is not closed in the momentum space (190). Second, the negligence of interband interaction leads to an apparent contradiction: The carrier compensation appears to be necessary for the nonsaturated MR according to Equation 3, but the Hall resistivity expressed by Equation 4 must be linearly dependent on the field when $n_e = n_h$, which is not true for most topological semimetals (e.g., see **Figure 2*a***). Third, according to Equation 3, even approximate electron-hole compensation should be able to lead to a quadratic or nearly-quadratic field dependence for ρ_{xx}. Such a dependence has indeed been observed in a number of topological semimetals (48, 183, 191–193), but linear or even sublinear MR has also been observed in a variety of samples (107, 171, 172, 174–180, 182, 183, 191, 194). Linear MR may be a classical effect due to strong current inhomogeneity (172) or may have a quantum mechanical interpretation (195) (see Section 3.2.8), while sublinear MR may be attributed to the weak antilocalization caused by strong SOC (196). With these considerations, the two-band model appears to be applicable only for a limited field range or at higher temperatures at which quantum effects are not significant.

Although obtaining the precise value of carrier mobility for individual bands might be challenging, the two-band model still provides an effective approach for the approximate description of magnetotransport properties of multiband materials. This model successfully explains the extremely large MR arising from high mobility and approximate carrier compensation. Then, a key question for topological semimetals is why Dirac/Weyl fermions have high mobility. This question can be understood in terms of the energy band characteristics of topological semimetals. Given that the carrier mobility is determined by relaxation time τ and effective mass m^*, i.e., $\mu = e\tau/m^*$, greater relaxation time and smaller effective mass favor higher mobility. As shown in Section 3.2.2, the cyclotron effective masses derived from quantum oscillations are indeed small for many topological semimetals, reaching as low as $0.02m_e$ (where m_e is the free electron mass) for some materials. Such massless behavior is naturally expected for ideal topological fermions since they are hosted by linearly dispersed bands crossing near the Fermi level, which requires zero mass in the Hamiltonian (11).

Greater relaxation time in topological materials may be associated with symmetry protection in many cases. For topological insulators, it has been well established that backscattering is forbidden by TRS, even though nonmagnetic defects exist, thus resulting in longer relaxation time

(197–201). In some topological semimetals, a strong suppression of backscattering due to nontrivial band topology has also been proposed (45); such suppression would lead to enhanced transport relaxation time. This idea is partially supported by the quantum oscillation studies that reveal a long quantum relaxation time in topological semimetals, as shown in Section 3.2.2.

3.2. Landau Quantization and Quantum Oscillations

In addition to the extremely large MR, another important phenomenon in the magnetotransport of topological semimetals is quantum oscillation (**Figure 2*b*,*c***), i.e., the Shubnikov–de Haas (SdH) effect. Quantum oscillations can also be probed in other measurements such as magnetization/magnetic torque [i.e., the de Haas–van Alphen (dHvA) effect], thermoelectric power, and ultrasonic absorption. Quantum oscillations have been widely used for the study of 3D topological insulators (202) and topological semimetals and reveal key parameters for Dirac/Weyl fermions such as effective mass, quantum mobility, and (most importantly) the Berry phase. In this section, we review quantum oscillation studies of topological semimetals.

3.2.1. The zeroth Landau level for relativistic fermions. Quantum oscillation theory for nonrelativistic electrons has been well established and documented in earlier textbooks and reviews (203, 204). Here we briefly recall the fundamental theory and put major emphasis on its extension to relativistic fermions. Quantum oscillation originates from the quantized cyclotron motion of charge carriers under magnetic fields, i.e., the Landau quantization of the energy states. With the conduction band splitting to Landau levels (LLs), the DOS at the Fermi level, DOS(E_F), becomes periodically modulated by magnetic field (more precisely, periodic in $1/B$), leading to periodic oscillations of physical quantities.

Panels *a* and *b* of **Figure 3** show the textbook drawings of the Landau quantization for spinless (i.e., ignoring Zeeman splitting) nonrelativistic electrons with parabolic dispersion. The quantized LL energy is $\varepsilon_n = (n + 1/2)\hbar\omega_c$, where $\omega_c = eB/m$ is the cyclotron motion frequency and the LL index $n = 0, 1, \ldots$. The energies of all LLs are field dependent and evenly spaced by $\hbar\omega_c$, as shown in **Figure 3*b***. For the lowest LL, a finite zero-point energy $\hbar\omega_c/2$ exists, which is in analogy to the zero-point energy of a harmonic oscillator. To distinguish the lowest LL for the nonrelativistic fermions from the exotic zeroth LL with field-independent zero energy for the relativistic fermions shown below, we rewrite the LL energy of nonrelativistic electrons as $\varepsilon_n = (n - 1/2)\hbar\omega_c$, where n becomes a nonzero integer $(1, 2, \ldots)$.

The LL quantization is completely different for the relativistic fermions with linear dispersion (**Figure 3*c***). Earlier studies on graphene (205, 206) established that the quantized energies of LLs for spinless 2D Dirac fermions are

$$\varepsilon_n = v_F \operatorname{sgn}(n)\sqrt{2e\hbar|B||n|} \quad (n = 0, \pm1, \pm2\ldots), \qquad 5.$$

where sgn(n) is the sign function and v_F is the Fermi velocity. As illustrated in **Figure 3*d***, LLs are no longer equally spaced for relativistic fermions given $\varepsilon_n \propto \sqrt{|n|}$. Most strikingly, a field-independent zeroth ($n = 0$) LL locked at the band crossing point ($\varepsilon_0 = 0$) appears, which is a signature unique to 2D relativistic electron systems. Such a zero energy can be understood in terms of the Berry phase arising from the cyclotron motion of carriers in momentum space (206). The detailed theoretical background of the Berry phase and its manifestation in transport measurements have been well understood (202, 207–209). In short, the Berry phase describes a geometrical phase factor of a quantum mechanical system acquired in the adiabatic evolution along a closed trajectory in the parameter space. Such a phase factor does not depend on the details of the temporal

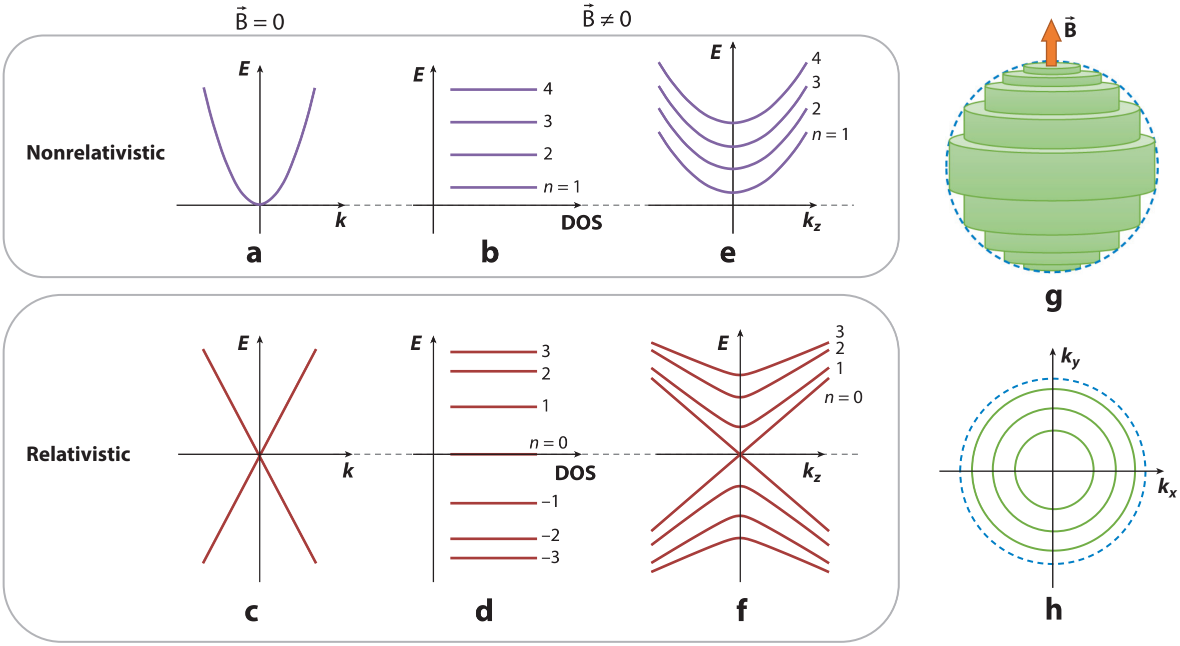

Figure 3

Landau quantization. (*a*,*c*) Schematics for energy-momentum dispersions of the (*a*) normal (nonrelativistic) and (*c*) relativistic electrons. (*b*,*d*) Landau spectra for the 2D spinless (*b*) nonrelativistic and (*d*) relativistic electrons. (*e*,*f*) Landau spectra for the 3D spinless (*e*) nonrelativistic and (*f*) relativistic electrons with the magnetic field along the k_z direction ($\boldsymbol{B}//k_z$). (*g*) Landau tubes intersecting a 3D spherical Fermi surface. (*h*) Landau rings within the 2D Fermi surface (ring). Panels *b*, *e*, and *g* show the scenario for nonrelativistic electrons without the zeroth Landau level.

evolution and thus differs from the dynamical phase. A nonzero Berry phase ϕ_B originates from the band touching point, such as Dirac nodes. Under magnetic fields, the cyclotron motion of Dirac fermions, i.e., the closed trajectory in momentum space, induces a Berry phase that changes the phase of quantum oscillations. Ideally, $\phi_B = \pi$ for an exact linear energy-momentum dispersion, and this value shifts when the bands deviate from linear dispersion and/or the Zeeman effect is strong (209, 210).

Before formulizing the quantum oscillation for relativistic fermions by incorporating the Berry phase–induced phase shift, we should pay attention to the dimensionality of the investigated material systems. The Landau quantization of the 2D surface state of topological insulators is very different from that of the Dirac or Weyl fermions in 3D topological semimetals. Most topological semimetals reported so far are 3D in nature [such as Cd_3As_2 (14, 127–130), Na_3Bi (13, 126), and the TaAs family (22, 23, 25, 27, 39, 86, 87, 211)], and 3D is necessarily required for a Weyl state (10). For nonrelativistic electrons in 3D, the motion along the magnetic field direction is not quantized, leading to additional energy of $(\hbar k_z)^2/2m$ (where k_z is the momentum along the magnetic field direction) for LLs:

$$\varepsilon_{n,k} = \frac{\hbar e B}{m^*}\left(n - \frac{1}{2}\right) + \frac{\hbar^2 k_z^2}{2m^*} \quad (n = 1, 2, 3, \ldots). \qquad 6.$$

Similarly, an additional energy term due to unquantized k_z also occurs for 3D relativistic fermions:

$$\varepsilon_n = v_F \,\mathrm{sgn}(n)\sqrt{2e\hbar|B||n| + (\hbar k_z)^2}. \qquad 7.$$

Therefore, although the zeroth LL's energy is still field independent, it is not strictly zero. Moreover, Equation 7 is valid for Dirac fermions with $n = 0, 1, 2, \ldots$. For Weyl fermions, the chirality is well defined due to the lifting of spin degeneracy, so Equation 7 needs to be modified for the zeroth LL of Weyl fermions. As discussed in Section 3.4, the chiral zeroth LL leads to one important effect for Weyl fermions, i.e., the chiral anomaly.

3.2.2. The Lifshitz–Kosevich model for de Haas–van Alphen oscillations. For the perfect 2D case, the Landau bands are degenerate into sharp levels (**Figure 3*b*,*d***), and the motions of all electrons at the Fermi level are in phase. For the 3D case, due to the additional energy related to unquantized k_z as shown in Equations 6 and 7, different LLs overlap in energy space, leading to a mixture of Landau bands for particular energy (**Figure 3*e*,*f***) and a continuous energy spectrum. This is better illustrated in **Figure 3*g***: Landau quantization for 3D free electrons manifests as Landau cylinders along the magnetic field direction, so an equal energy surface intersects multiple Landau cylinders. This scenario is distinct from the 2D case (**Figure 3*b***). Therefore, different models have been derived for 3D and 2D quantum oscillations.

Here we start with the dHvA oscillation because the magnetization is the derivative of the Gibbs thermodynamic potential Ω at constant temperature and chemical potential ζ, $M = -(\frac{\partial \Omega}{\partial B})_{T,\zeta}$, so that it directly reflects the LL spectrum. At the zero-temperature limit, the oscillatory thermodynamic potential Ω due to Landau quantization for a 3D system can be expressed as (in CGS units) (203)

$$\Omega_{\text{osc}} = \left(\frac{e}{2\pi c\hbar}\right)^{3/2} \frac{e\hbar B^{5/2}}{mc\pi^2(\partial^2 S_{\text{extr}}/\partial k_z^2)^{1/2}} \sum_{r=1}^{\infty} \frac{1}{r^{5/2}} \cos\left[2\pi r\left(\frac{F}{B} - \gamma\right) + 2\pi\delta\right], \qquad 8.$$

where S_{extr} is the extremal Fermi surface cross-section area perpendicular to the magnetic field, $\partial^2 S_{\text{extr}}/\partial k_z^2$ is the Fermi surface curvature along the k_z direction (i.e., the field direction) at the extremal cross section, and r is the harmonic index. Given several damping factors, the general formula of the magnetization oscillations for a 3D system, derived by Lifshitz & Kosevich (the LK formula) (203, 204, 212), is (in SI units)

$$M_{\text{osc}}^{3\text{D}} = -\left(\frac{e}{2\pi\hbar}\right)^{3/2} \frac{S_{\text{extr}}}{\pi^2 m^*} \left(\frac{B}{|\partial^2 S_{\text{extr}}/\partial k_z^2|}\right)^{1/2} \sum_{r=1}^{\infty} \frac{1}{r^{3/2}} R_{\text{T}} R_{\text{D}} R_{\text{S}} \sin\left[2\pi r\left(\frac{F}{B} - \gamma + \frac{\delta}{r}\right)\right]. \qquad 9.$$

R_{T}, R_{D}, and R_{S} are the temperature-, field-, and spin-damping factors, which are associated with the finite temperature corrections to the Fermi-Dirac distribution function, the finite relaxation time due to impurity scattering, and the phase difference between the spin-up and spin-down subbands, respectively. These factors can be expressed as

$$R_{\text{T}} = \frac{raT\mu/B}{\sinh(raT\mu/B)}, \qquad 10.$$

$$R_{\text{D}} = \exp\left(-\frac{raT_{\text{D}}\mu}{B}\right), \qquad 11.$$

$$R_{\text{S}} = \cos\frac{r\pi g\mu}{2}, \qquad 12.$$

where μ is the ratio of effective cyclotron mass m^* to free electron mass m_0. T_{D} is the Dingle temperature that is relevant to the quantum relaxation time, and $a = (2\pi^2 k_{\text{B}} m_0)/(\hbar e) \approx 14.69$ T/K.

The sine term in Equation 9 describes the oscillation with frequency rF and phase factor $2\pi r(-\gamma + \frac{\delta}{r})$, where the fundamental frequency F is linked to S_{extr} by the Onsager relation

$F = \hbar S_{\mathrm{extr}}/2\pi e$. The determination of the phase factor is of particular interest for the quantum oscillation study of topological materials since the Berry phase ϕ_{B} is connected to the phase factor via $\gamma = \frac{1}{2} - \frac{\phi_{\mathrm{B}}}{2\pi}$. The Berry phase, which was not included in Lifshitz & Kosevich's original formalism (i.e., $\gamma = \frac{1}{2}$) (212), can effectively shift the phase of quantum oscillations (209, 210). The phase shift δ in Equation 9, which is determined by the dimensionality of the Fermi surface, is 0 for the 2D case and $\pm 1/8$ for the 3D case. For the 3D case, $\delta = -1/8$ ($\delta = +1/8$) for maximal (minimal) cross section for a 3D electron pocket (203, 204, 212) and a 3D hole pocket, respectively.

Although most topological semimetals are 3D, there are also some materials with layered structure and that thus display a quasi-2D electronic structure, such as ZrSiTe (156) and (Sr/Ba)Mn(Bi/Sb)$_2$ (143, 173, 177, 213). For a perfectly 2D system, the above LK formula has been modified by Shoenberg and others (203, 204, 214, 215):

$$M_{\mathrm{osc}}^{\mathrm{2D}} = -\left(\frac{e}{2\pi\hbar}\right)\frac{S}{\pi^2 m^*}\sum_{r=1}^{\infty}\frac{1}{r}R_{\mathrm{T}}R_{\mathrm{D}}R_{\mathrm{S}}\sin\left[2\pi r\left(\frac{F}{B}-\gamma\right)\right], \qquad 13.$$

with the same definitions for damping factors (R_{T}, R_{D}, and R_{S}) and phase factor γ as the 3D model. The Fermi surface cross-section area becomes a constant for 2D, so S_{extr} in the 3D model (Equation 9) is replaced by S, and the phase factor δ is zero. In addition to this phase difference, the oscillation amplitude (i.e., the prefactor of the summation in Equation 13) and harmonic components ($r \neq 0$) are enhanced relative to the 3D model.

Significantly, the above 3D (Equation 9) and 2D (Equation 13) LK models are based on the assumption of constant chemical potential, which is appropriate for a 3D system because the electron energy spectrum is continuous, as mentioned above. In this scenario, the lowest unoccupied state is always located at E_{F} and is independent of B (i.e., the chemical potential $= E_{\mathrm{F}}$ for $T =$ 0 K). In contrast, the 2D Landau quantization gives rise to discrete energy levels, so the chemical potential, which is the minimum energy needed to add an electron to the system, is pinned to the highest occupied LL and hence also oscillates with ramping magnetic field. This chemical potential oscillation will affect the quantum oscillations. Furthermore, in real materials, the interlayer coupling is not negligible in layered compounds and is also not captured by Equation 13. More comprehensive analyses can be found in References 203 and 204 and references therein.

In practice, the oscillation frequency or frequencies F can be directly resolved from the fast Fourier transform (FFT) of the oscillation pattern, and other important parameters, including the effective cyclotron mass, quantum relaxation time, and Berry phase, can be obtained from the analyses with the LK formula. From FFT, one can also clarify whether the higher harmonic terms ($r > 1$) with frequency rF are significant. In principle, these terms attenuate quickly with $r^{-3/2}$ for a 3D system (Equation 9) or r^{-1} for a 2D system (Equation 13), and thus the quantum oscillations in real materials are usually dominated by fundamental frequencies ($r = 1$). If the oscillation contains only a single frequency without obvious harmonic frequency components, effective mass m^* can be obtained from the fit of the temperature dependence of the oscillation amplitude A_{osc} at a fixed magnetic field to the thermal damping factor R_{T} in Equation 10 [i.e., $M_{\mathrm{osc}}(T) \propto R_{\mathrm{T}}$]. In normal metals with exact parabolic bands, the band effective mass is expected to be a constant, despite the location of Fermi level. It can be easily shown that such band mass is equivalent to the cyclotron mass, which is defined as $m^* = \frac{\hbar^2}{2\pi}\left[\frac{\partial S}{\partial E}\right]_{E=E_{\mathrm{F}}}$ within the semiclassical approximation, where S is the extremal area enclosed by the cyclotron orbit in momentum space. Applying the same definition to the linearly dispersed bands with an isotropic Dirac cone, one can easily find that m^* is connected to the Fermi vector k_{F} and velocity v_{F} with $m^* = \hbar k_{\mathrm{F}}/v_{\mathrm{F}}$. Thus, m^* should vanish when a Dirac point resides at E_{F} (where $k_{\mathrm{F}} = 0$) and should increase when the Dirac point is shifted away from E_{F}. Such a trend has been observed in various Dirac materials (172, 216). Generally, E_{F} is not too far away from the Dirac band crossing point in most known topological semimetals, so m^* obtained from quantum oscillation is usually small, as summarized in **Table 1**.

With a known effective mass, the Dingle temperature that is associated with the quantum relaxation time can be extracted from the fit of the field dependence of the oscillation amplitude at a fixed temperature by the field damping factor R_D in Equation 11 [i.e., $M_{osc}(B) \propto R_D$]. Because T_D is included in the exponential term of R_D, the logarithm of the oscillation amplitude normalized by $B^{1/2}R_T$ (for 3D) or R_T (for 2D) should have linear dependence on $1/B$ according to Equation 11. Thus, T_D can be obtained from the slope of the linear fit of such a Dingle plot. In practice, Dingle plots are nonlinear in some cases in which accurate T_D cannot be obtained. Such a scenario could be attributed to, e.g., sample inhomogeneity, magnetic field inhomogeneity, a beating oscillation pattern due to the existence of two very close frequencies, or torque interaction at high fields if torque magnetometry is used (203).

From T_D extracted from a Dingle plot, the quantum relaxation time τ_q can be derived via $\tau_q = \hbar/(2\pi k_B T_D)$. Because τ_q affects the oscillation amplitude exponentially (Equation 11), strong dHvA oscillations present in low field ranges implies large τ_q, which is generally the case for topological semimetals (**Table 1**). It is important to distinguish the quantum relaxation time from the transport relaxation time τ_t, as discussed in Section 3.1. While both arise from the scattering by static impurities and defects, these two quantities are essentially different (217, 218): τ_q characterizes the quantum lifetime of the single-particle relaxation time of the momentum eigenstate, which determines the LL broadening of the momentum eigenstate by $\Gamma = \hbar/2\tau_q$, whereas τ_t is introduced in the classical Drude model and affects the Drude conductivity, $\sigma = ne\mu = ne^2\tau_t/m^*$. Given that τ_t measures the motion of charged particles along the electric field gradient, it is largely unaffected by the forward scattering (i.e., small-angle scattering), in contrast to τ_q, which is susceptible to momentum scattering in all directions. Therefore, τ_t is usually larger or even much larger than τ_q. Taking the form of the classical transport mobility $\mu_t = e\tau_t/m^*$, one can also define the quantum mobility by $\mu_q = e\tau_q/m^*$. Consequently, μ_q obtained from quantum oscillation is usually less than μ_t derived from magnetotransport, as observed in various topological semimetals (see **Table 1**).

In addition to nearly zero effective mass and high quantum mobility, nontrivial Berry phase is a key signature of relativistic fermions. As indicated above, it results in the zeroth LL, which is absent in the LL spectrum of nonrelativistic electrons. In general, for a system exhibiting quantum oscillations with a single frequency, ϕ_B can be determined from the LL index fan diagram, i.e., the plot of the LL indices n versus the inverse magnetic field $1/B$ (one example is shown in **Figure 4*a*,*b***). This method has been widely used in previous studies on topological insulators, and a proper way to construct a LL fan diagram has been established, although there had been some confusion in early studies (202, 219). We first consider a 2D situation. As shown in **Figure 3*b***, with ramping magnetic field, the LLs successively pass through E_F. Integer LL indices are assigned when E_F lies at the middle of two adjacent LLs [i.e., minimum DOS(E_F)], while half-integer indices are assigned when E_F is right at the LL [maximum DOS(E_F)]. For a LL fan diagram established with such a definition of the LL index, the linear extrapolation of the linear fit of $n(1/B)$ to the $\frac{1}{B} \rightarrow 0$ limit must lead to $n = 0$ for nonrelativistic electrons, but $n = 1/2$ for relativistic fermions due to the zeroth LL pinned at the zero energy. This $n = 1/2$ intercept corresponds to an ideal Berry phase of π. For a 3D system, the phase of quantum oscillation is shifted by $2\pi\delta$, as mentioned above, so the linear extrapolation should intercept the n axis at $\frac{\phi_B}{2\pi} - \delta$.

Therefore, proper assignment of LL indices is critically important for guaranteeing precise determination of the Berry phase. Oscillations in differential magnetic susceptibility $\chi (= \frac{dM}{dB})$ offer a straightforward approach to determining integer LL indices; that is, the minima of χ should be assigned with integer LL indices, since they correspond to minimal DOS(E_F). This scenario can

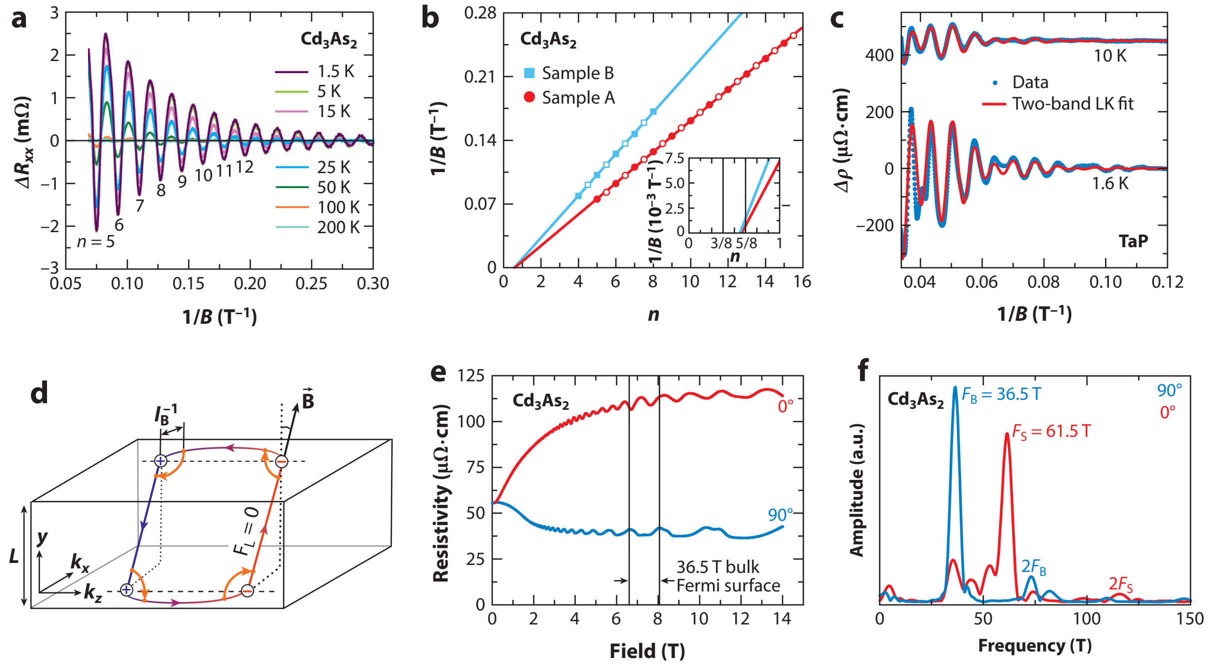

Figure 4

Quantum oscillations in topological semimetals. (*a*) The oscillatory component of resistance for Cd_3As_2, obtained via subtracting the smooth magnetoresistance (MR) background, as a function of $1/B$ at various temperatures. (*b*) Landau level (LL) fan diagram constructed from Shubnikov–de Haas oscillations for two Cd_3As_2 samples. (*Inset*) Intercepts of the linear extrapolations of LL indices for the two samples. (*c*) The oscillatory component of resistance for TaP, obtained via subtracting the smooth MR background, as a function of $1/B$ at various temperatures. The red solid lines show the fits of the oscillation data to the two-band Lifshitz–Kosevich (LK) model. (*d*) Mixed real and momentum space representation of the Weyl orbit, which consists of the Fermi arcs at the top and bottom surfaces connecting the projections of Weyl nodes with opposite chirality (labeled as + and −, respectively) and the bulk states with fixed chirality (*blue* and *red*). (*e*,*f*) MR at 2 K and its fast Fourier transform for a thin (150-nm) slab sample, for magnetic field parallel (90°) and perpendicular (0°) to the surface. In addition to the bulk frequency F_B, another oscillation frequency corresponding to the surface state (F_S) is observed for the perpendicular field. Panels *a* and *b* adapted with permission from Reference 178. Copyright 2014, American Physical Society. Panel *c* adapted from Reference 192 under a Creative Commons Attribution 4.0 International License. Panels *d*–*f* adapted from Reference 44 with permission from Springer Customer Service Centre GmbH, copyright 2016.

be understood as follows: As indicated above, magnetization is equal to the derivative of the Gibbs thermodynamic potential Ω at constant temperature and chemical potential ζ, $M = -(\frac{\partial \Omega}{\partial B})_{T,\zeta}$. At zero temperature, Ω is indeed proportional to the total energy of electrons and is modulated by magnetic field in the form of a cosine function (Equation 8) (203). Given $\chi = \frac{\partial M}{\partial B} = -\frac{\partial^2 \Omega}{\partial B^2}$, χ and Ω would oscillate in phase when Landau quantization occurs with increasing magnetic field. Since the minima of Ω correspond to the minimal DOS(E_F), minimal χ should be assigned with integer LL indices. Given $\chi = \frac{\partial M}{\partial B}$, if the oscillations of magnetization are used to establish a LL fan diagram, the minima of M should be assigned with $n - 1/4$ (where n is an integer number). With this approach, the nontrivial Berry phase has been extracted from dHvA oscillations for several topological semimetals (156, 220–222).

Several factors can affect the value of the Berry phase in topological semimetals. First, the Berry phase can deviate from an ideal value of π if the band dispersion is not perfectly linear (210). Second, the Zeeman effect, which has not been considered so far, also leads to a deviation of the Berry phase obtained from a LL fan diagram (210). Therefore, the Berry phase determination using the LL fan diagram should be performed with caution for high-field quantum oscillations or for materials with large g-factors such as Cd_3As_2 (172, 223) and ZrSiS (221). Furthermore, from the aspect of data analysis, reading the Berry phase from a LL fan diagram may bear large uncertainty in some cases. Because the Berry phase is determined by the intercept of the linear fit of $n(1/B)$, when low-LL indices cannot be reached in experiments due to high oscillation frequency, a slight change in the slope of the linear fit can lead to a large shift in the intercept, thus resulting in a large uncertainty in the extracted Berry phase. Therefore, reaching low-LL indices under high magnetic fields is necessary for obtaining a reliable Berry phase from a LL fan diagram.

In addition to magnetization measurements, dHvA oscillations can also be probed by torque magnetometry since a magnetic moment $\vec{m}$ in a magnetic field is subject to a torque $\vec{\tau} = \vec{m} \times \vec{B}$. It is convenient to perform magnetic torque measurements on topological semimetals by using a cantilever (176, 224–230) to high magnetic field, even up to 60 T. One drawback of the torque magnetometry is the torque interaction, an instrumental effect due to the feedback of the oscillating magnetic moment on the cantilever position, which leads to artificial effects in quantum oscillations under high magnetic fields (203).

3.2.3. Shubnikov–de Haas oscillations. Besides dHvA oscillation, the resistivity oscillation, i.e., the SdH effect, is also widely used to study topological semimetals (46, 141, 171, 172, 174, 178, 179, 183, 191–193, 231–233). The extraction of the Berry phase from SdH oscillations seems straightforward. Since the SdH effect also originates from Landau quantization, the nontrivial Berry phase associated with the zeroth LL also manifests itself by a phase shift in the SdH oscillation. As stated above, integer LL indices should be assigned when E_F lies in the middle of two adjacent LLs and DOS(E_F) reaches minima. The situation is less complicated in 2D integer quantum Hall systems (including the 2D surface states of the 3D topological insulators), in which the integer LL indices unambiguously correspond to the quantized Hall plateaus where the longitudinal conductance reaches minima ($S_{xx} = 0$) due to the dissipationless edge state. The proper way to build a LL fan diagram from the SdH effect for topological insulators was discussed in a previous review (202).

In the studies of topological semimetals, however, there have been controversies in constructing LL fan diagrams from the SdH effect. The literature contains various definitions for integer LL indices, including resistivity minimum (141, 178, 234, 235), resistivity maximum (171, 179, 183, 191, 193, 232, 233, 236–239), and conductivity minimum (143, 172, 213). At first glance, it is natural to extend the above argument for the quantum Hall system to topological semimetals, except that the conductivity of topological semimetals cannot be directly measured through conventional transport experiments but should be obtained through inverting the resistivity tensor, $\hat{\sigma} = \hat{\rho}^{-1}$. For in-plane ($x$-$y$ plane) current $\boldsymbol{I}$ and out-of-plane (z-direction) magnetic field $\boldsymbol{B}$ (i.e., a standard Hall effect setup with $\boldsymbol{B} \perp \boldsymbol{I}$) applied to a 2D system, the charge carriers undergo only in-plane motion, and we have

$$\hat{\sigma} = \begin{pmatrix} \sigma_{xx} & \sigma_{xy} \\ \sigma_{yx} & \sigma_{yy} \end{pmatrix} = \hat{\rho}^{-1} = \begin{pmatrix} \rho_{xx} & \rho_{xy} \\ \rho_{yx} & \rho_{yy} \end{pmatrix}^{-1}. \qquad 14.$$

Here the resistivity tensor elements ρ_{ij} ($i,j = x, y$) are defined as E_i/J_j (where E_i is the electric field component along the $+i$ direction and J_j is the current density along the $+j$ direction) or, equivalently, V_i/I_j (where V_i is the voltage drop along the $+i$ direction and I_j is the current along the $+j$ direction). In fact, from this definition, ρ_{xx} and ρ_{xy} are essentially the longitudinal and transverse (Hall) resistivity. Under the assumption of isotropic scattering rate for a given 2D material, it is easy to demonstrate $\rho_{xx} = \rho_{yy}$ and $\rho_{xy} = -\rho_{yx}$. Therefore, precise conductivity can be obtained from measured ρ_{xx} and ρ_{xy} via $\sigma_{xx} = \frac{\rho_{xx}}{\rho_{xx}^2+\rho_{xy}^2}$.

However, additional considerations must be taken for 3D topological semimetals. Although the integer quantum Hall effect (QHE) also has a semiclassical interpretation based on Landau quantization, its underlying transport mechanism is distinct from the SdH effect due to its nonlocal character. As discussed in more detail in Sections 3.2.7 and 3.5, the quantized Hall conductance plateaus and the zero longitudinal conductance are associated with the dissipationless edge channels. Such scale-invariant dissipationless edge conduction in quantum Hall systems is completely different from the transport in conventional diffusive systems, where the resistance or conductance is associated with the sample dimensions and is governed by the transport relaxation rate (i.e., the scattering rate). The scattering mechanisms in real materials can be very complicated. Fortunately, a semiquantitative LK model that gives satisfactory descriptions for the SdH effect has been developed for 3D systems. The earlier transport theory established that the scattering probability is proportional to the number of available states that electrons can be scattered into (47, 240), and the scattering possibility thus oscillates in concert with the oscillations of DOS(E_F) and gives rise to SdH oscillations (203, 204). More explicitly, $\mathrm{DOS}(E_F)_{osc} \propto (\frac{m^*B}{S_{extr}})^2 \frac{\partial M_{osc}}{\partial B}$. With this relation, the expression for conductivity/resistivity oscillation, i.e., the LK formula for the SdH effect, can be derived from the derivative of the magnetization oscillation (203, 204). Clearly, within the framework of this LK model based on the oscillation scattering rate, conductivity should exhibit maxima when the scattering rate reaches minima that occur at minimal DOS(E_F). Given that integer LL indices should correspond to DOS(E_F) minima as indicated above, the maxima of conductivity oscillation should be assigned with integer LL indices. However, this approach is based on the semiquantitative model for the SdH effect (203). The scattering rate in a real material depends on a number of factors and can be very complicated, particularly in multiband or anisotropic systems, which could lead the SdH oscillations to strongly deviate from the LK theory (204). As a result, a simple connection between the integer LL indices and the SdH oscillation extrema may be problematic in some cases. Therefore, to demonstrate the nontrivial Berry phase, a better approach might be the oscillation of thermodynamic properties that are directly linked to the LL energy spectrum, such as the dHvA effect as discussed above.

In addition, the complication of the scattering rate in the SdH oscillation also leads to inconsistency between the SdH effect and the dHvA effect. In some layered topological semimetals, dHvA oscillation is strong for arbitrary magnetic field directions, but SdH oscillation quickly attenuates when the magnetic field is tilted toward the current direction (221, 226, 232, 241, 242). In those materials, the stronger dHvA effect is also useful in distinguishing the Zeeman splitting effect from the oscillation pattern (221).

3.2.4. Multifrequency quantum oscillations. The above discussions on LL fan diagrams are applicable to quantum oscillations with a single frequency. However, multiple oscillation frequencies are often observed in most topological semimetals, such as those of the TaAs family (179, 180, 182, 183, 191–193, 227, 243) and *WHM* materials with PbFCl-type structure (W = Zr or Hf; H = Si, Ge, or Sn; M = S, Se, or Te) (156, 221, 222, 226, 228, 232, 233, 241, 242, 244, 245). Given $F = \hbar S_{extr}/2\pi e$, the dependence of oscillation frequencies on the magnetic field orientation provides useful information on Fermi surface morphology. In the presence of multifrequency oscillations, the method used to analyze effective mass, quantum mobility, and the Berry phase differs from what is discussed for the single-frequency situation. The commonly used approach to obtain the effective mass for each frequency band is the fits of the FFT amplitudes for each frequency component by the thermal damping factor R_T (Equation 10). In this method, the inverse magnetic field $\frac{1}{B}$ in R_T is approximated by the average inverse field $\langle\frac{1}{B}\rangle$, defined as $\langle\frac{1}{B}\rangle = \frac{1}{2}(\frac{1}{B_1} + \frac{1}{B_2})$, where $\frac{1}{B_1}$ and $\frac{1}{B_2}$ are the upper and lower inverse fields used for FFT analyses. However, this method may lead to large errors for the fitted effective mass in some cases, since the obtained effective mass may depend on the range of the inverse magnetic field ($\frac{1}{B_1} \rightarrow \frac{1}{B_2}$) used for FFT. For example, for the NLSM ZrSiS, the effective mass obtained from the fit of the FFT amplitude is greatly increased when a narrower field range is used for the FFT analysis. When the inverse magnetic field range is taken as 0.143–1.5 T^{-1}, the fitted effective mass is small for the $F_\beta = 240$ T band, $\sim 0.052\ m_0$ (221). However, when the inverse field range is reduced to 0.3–0.5 T^{-1}, the fitted effective mass is increased to 0.17 m_0 (A. Carrington, private communication). Since the two quantum oscillation frequencies observed in ZrSiS (i.e., 8.4 T and 240 T) are far apart, the effective masses corresponding to these oscillation components can also be obtained by fitting the temperature dependence of the oscillation amplitude probed at a certain field. The effective mass obtained using such a method is 0.18 m_0 for the 240 T oscillation component. This example shows that a narrower inverse field range for FFT may improve the accuracy of the fitted effective mass. However, this is not always true. Therefore, one must be extremely careful when using FFT amplitudes to extract the effective mass. For multifrequency oscillations, if the frequencies are far apart, it may be possible to obtain an accurate effective mass by directly reading the oscillation amplitudes, as discussed above. In contrast, if the frequencies are close to each other, several approaches may be used to double check effective mass (A. Carrington, private communication). First, as demonstrated above, accurate effective masses may be obtained from the FFT analyses within a narrow field range. Second, it may be possible to use Fourier filters to separate multifrequency oscillations into several single-frequency oscillations, which may allow one to obtain an accurate effective mass for each frequency. In this method, the data near the two ends of the magnetic field range should be excluded after applying the Fourier filter, since the end effect could induce artificial signal. To minimize the errors in effective mass, the combination of the above methods, together with a simulation of the oscillation pattern using the LK formula after obtaining the effective mass, may be helpful.

The Dingle temperature and Berry phase can be extracted through fitting the oscillation pattern to the generalized multiband LK formula, with the assumption that the quantum oscillations of different bands are additive. This method was previously used for the $LaAlO_3/SrTiO_3$ heterostructure (246) and was first employed for analyzing the SdH oscillations of TaP (**Figure 4*c***) in the study of topological semimetals (192) and was then proven to be effective in characterizing topological fermion properties for many other multiband topological semimetals (143, 156, 221, 226, 230, 245, 247–249). For the multiband LK fit, it is important to include all major frequency components, as well as the higher harmonic ($r > 1$ in Equations 9 and 13) terms if they are significant in the FFT spectrum, although there is a trade-off for accuracy due to the increased number of parameters. R_S is field independent (see Equation 12) and can thus be treated as a constant for the fit; it takes effects in modulating the amplitude for the harmonic component, as it contains r. Furthermore, R_S can be used to extract the Landé g-factor of a 2D/quasi-2D system via the spin-zero method; that is, the oscillation amplitude vanishes at some field orientation due to the interference of spin split Fermi surfaces. This provides an alternative method to evaluate the g-factor in addition to the direct measurement of the separation of the split oscillation peaks. Such analysis has been reported for ZrSiS (221) and WTe_2 (250).

3.2.5. Magnetic breakdown. Multiple oscillation frequencies usually result from multiple Fermi surface extremal cross-section areas perpendicular to the field. Additionally, charge carriers may tunnel from one cyclotron orbit to another and jump back to the original one to form a bigger cyclotron orbit, hence leading to an additional frequency or frequencies equal to the sum or difference of two or more fundamental frequencies (203, 251). This phenomenon, termed magnetic breakdown, becomes more pronounced at high fields because the tunneling probability scales exponentially with the inverse field $1/B$ as $e^{-\alpha/B}$, where α is a material-dependent parameter relevant to the k-space separation of the orbits (203). The additional frequencies ascribed to magnetic breakdown have been observed in high-field quantum oscillation studies on several topological semimetals (171, 226, 252).

In type II WSMs, the magnetic breakdown has been predicted to be associated with the Klein paradox, which states that the tunneling barrier is nearly "transparent" for relativistic fermions when its height exceeds the electron's rest energy mc^2 (253). This relativistic effect is attributed to the positron or electron emission by a potential barrier when the barrier is sufficiently high (254–256). The matching between electron and positron wave functions across the barrier leads to high-probability tunneling (257). However, the requirement of the high potential barrier ($\sim mc^2$) imposes a great challenge for the experimental observation of this phenomenon in particle physics. Fortunately, the massless relativistic fermions discovered in condensed matter provide a realistic platform, given that, in principle, there is no theoretical requirement of the potential barrier for massless relativistic fermions. Klein tunneling has been demonstrated in graphene, with a potential barrier created by a local gate (257, 258). A similar effect is expected in topological semimetals with massless relativistic fermions. Recent theoretical work has predicted a momentum space counterpart of Klein tunneling in quantum oscillations for type II WSMs (259). In the scenario of magnetic breakdown, quantum tunneling through different momentum space orbits naturally mimics real space tunneling of carriers [e.g., in graphene (257, 258)], which is expected to lead to an unusual dependence of the FFT amplitude on magnetic field orientation (259).

3.2.6. Quantum oscillation due to Weyl orbits. The unusual surface Fermi arc is one distinct property of topological WSMs. For a DSM whose Dirac node can be viewed as the superposition of two Weyl nodes with opposite chirality, its surface state exhibits two sets of Fermi arcs curving in opposite directions on two opposite surfaces, as shown in **Figure 4*d***. It has been predicted that under magnetic fields, electrons can transport on a cyclotron orbit that connects one surface Fermi arc to the opposite Fermi arc by coupling to bulk states (**Figure 4*d***) (43, 260). Such an unconventional Weyl orbit manifests itself by an additional frequency in quantum oscillations (**Figure 4*e*,*f***), with 2D character that can be verified by the measurement of the field orientation dependence of oscillation frequency (i.e., $F \propto 1/\cos\theta$). Quantum oscillations due to Weyl orbits exhibit anomalous properties such as a sample thickness–dependent phase shift. To observe such a Weyl orbit, it is necessary to reduce the sample size to suppress the contribution of the bulk states. This has been demonstrated in nanostructures of Cd_3As_2 (**Figure 4*e*,*f***) (44, 261) and WTe_2 (262).

3.2.7. Other anomalous transport signatures originating from the zeroth Landau level. As indicated above, the field-independent zeroth LL of relativistic fermions leads to a phase shift in quantum oscillations from which the Berry phase can be inferred. In some layered topological semimetals, the zeroth LL has been probed more directly by several transport techniques such as QHE and interlayer tunneling.

The concept for QHE for 2D Dirac fermions has already been established for graphene and topological insulators (216, 263–265). Under a magnetic field, Landau quantization gives rise to quantized electron cyclotron orbits. Semiclassically, under sufficiently strong field, the electrons are pinned to these quantized small radii orbits, which causes a bulk insulating state. However, electrons that are close enough to the edges cannot complete cyclotron motions but rather get bounced back by the edges. Given the direction of the Lorentz force, the reflected electrons have to move forward until they are reflected by the edge again. This creates the so-called skipping orbit at the edge that carries current, i.e., the edge channel (**Figure 5*a***). Given that the

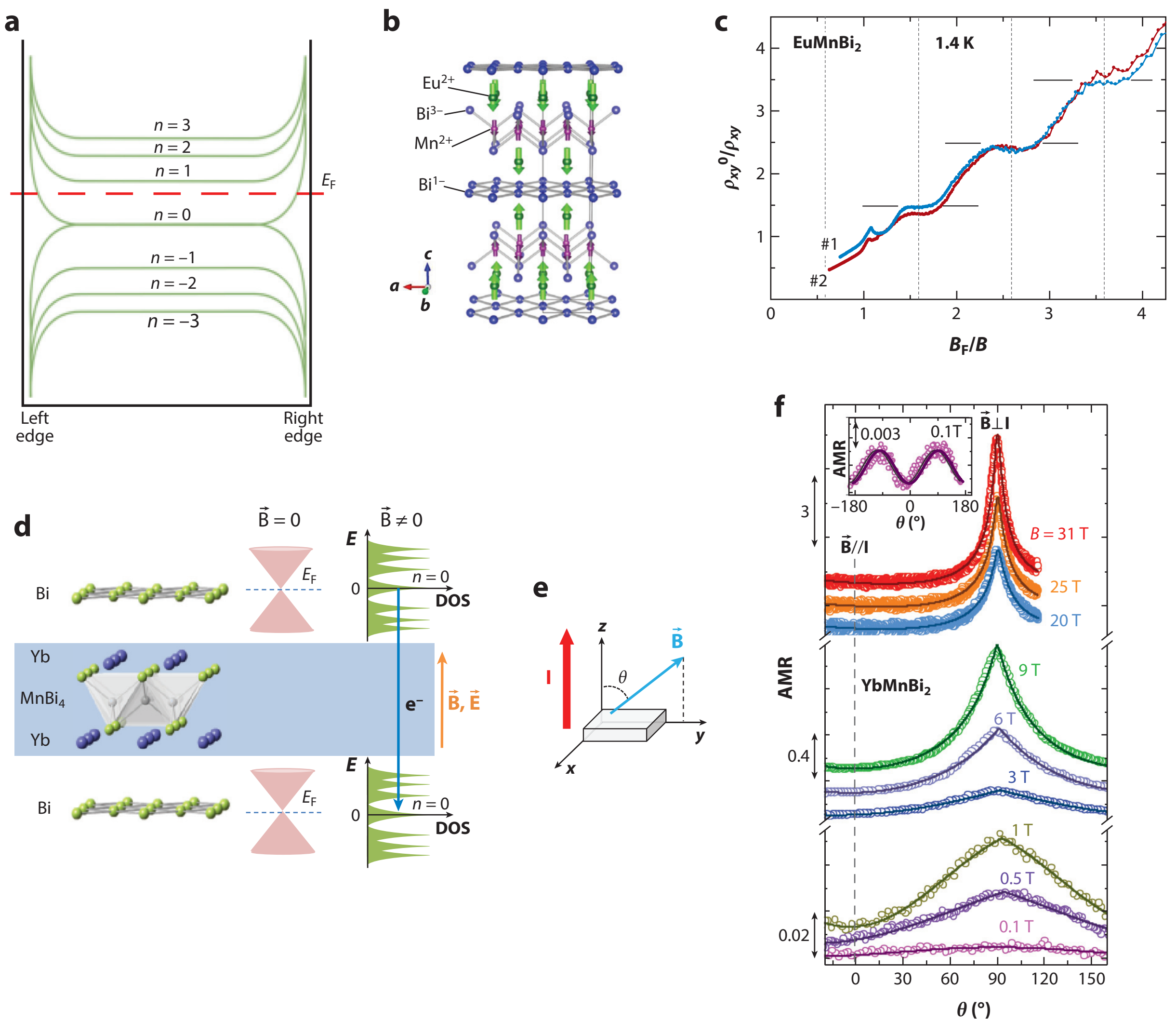

Figure 5

Direct manifestations of the zeroth Landau level (LL). (*a*) Schematic of the real space Landau levels for relativistic electrons in a finite-size 2D sample. (*b*) Crystal structure of $EuMnBi_2$. (*c*) Normalized inverse Hall resistivity $\rho_{xy}{}^0/\rho_{xy}$ versus B_F/B measured at 1.4 K for two $EuMnBi_2$ samples, where B_F is the SdH oscillation frequency and $B = \mu_0(H + M)$ is the magnetic induction. (*d*) Schematic of the interlayer tunneling of the zeroth LLs' relativistic fermions in $YbMnBi_2$. (*e*) Experimental setup for the measurement of the angular dependence of interlayer magnetotransport. (*f*) Angular-dependent interlayer resistance (AMR) measured under different fields up to 31 T and at $T = 2$ K, using the setup in panel *e*. The darker curves superimposed onto the data represent the fits to the tunneling model. The inset shows the $\sin^2\theta$ dependence at low field. Panels *b* and *c* adapted from Reference 177 under a Creative Commons Attribution 4.0 International License. Panels *d–f* adapted from Reference 247 under a Creative Commons Attribution 4.0 International License.

skipping orbit originates from the cyclotron orbit, the number of the edge conduction channels is determined by the number of the quantized cyclotron motion states that electrons can occupy, which is the number of the filled LLs below E_F. This gives rise to quantized Hall conductance of $G_{xy} = nG_0$, where $G_0 = e^2/h$ is the conductance quantum. In the language of band theory, the internal (bulk) of the 2D system is gapped when E_F locates in between LLs. At the sample edge, the confining electrostatic potential that keeps electrons inside the sample bends the LLs upward, as illustrated in **Figure 5*a***. The bent LLs that cross E_F form the edge channels, giving rise to quantized Hall conductance. From the above edge channel interpretation for the QHE, the QHE is a direct manifestation of Landau quantization of electron energy states. This is in contrast with SdH oscillation, which arises from the oscillating scattering rate and is thus an indirect probe of LLs. In other words, the QHE is a nonlocal transport phenomenon due to LLs, while the SdH effect is a manifestation of LLs in local transport. Furthermore, the QHE also has a topological interpretation, which is discussed in Section 3.5.

Given the existence of the field-independent zeroth LL pinned at the band crossing point (**Figure 3*d,f***), there is always an edge channel formed by the zeroth LL, as shown in **Figure 5*a***. Since the zeroth LL is evenly shared by both electrons and holes (**Figures 3*f*** and **5*a***), the contribution of the zeroth LL to edge conduction is half the contribution of nonzero LLs, leading to the so-called half-integer quantization; i.e.,

$$G_{xy} = G_0 \left(n + \frac{1}{2} \right). \qquad 15.$$

This half-integer quantization can also be understood in terms of a Berry phase of π for relativistic fermions and has been observed in graphene (216, 263), zero-gap HgTe quantum wells (266), and 3D topological insulators (264, 265). In real materials, an integer factor may be applied for G_0 due to degeneracy, such as graphene with a factor of 4 that originates from spin and valley degeneracies (216, 263).

Given the difference in Landau quantization in 2D and 3D systems as mentioned in Section 3.2.1, it is challenging to probe the half-integer QHE in 3D topological semimetals. One approach is to pursue their 2D nanostructures, but only the integer QHE has been observed so far in nanostructures of Cd_3As_2 and WTe_2 (261, 267, 268), probably due to the quantum confinement effect, which gaps the Dirac cone (267). Masuda et al. (177) reported a half-integer QHE in a bulk DSM $EuMnBi_2$ with a layered structure (**Figure 5*b***). This material exhibits the coexistence of two AFM orders: one formed by the Mn sublattice and the other by the Eu sublattice. Application of a magnetic field induces a spin flop transition for the Eu AFM order, resulting in a canted AFM state, which significantly reduces interlayer coupling so that Dirac fermions generated by Bi square-net layers are more confined within the plane (i.e., are quasi-2D) and exhibit signatures of the half-integer QHE. As seen in **Figure 5*c***, $1/\rho_{xy}$ normalized by $1/\rho_{xy}{}^0$ (where $\rho_{xy}{}^0$ is the step size of successive plateaus) displays quantized plateaus with half-integers. However, the quantum limit corresponding to $(1/\rho_{xy})/(1/\rho_{xy}{}^0) = 1/2$ could not be reached in this system because the canted AFM state of Eu sublattice exists only in a limited field range.

In another structurally similar compound, $YbMnBi_2$, the zeroth LL was probed via interlayer transport (247). In this material, the Bi layers that host relativistic fermions are separated by the relatively insulating Yb-MnBi-Yb blocks, leading to a quasi-2D electronic state. As shown in **Figure 5*d***, given that two linear bands cross right at E_F in this material (269), 2D Landau quantization leads to the zeroth LL to be pinned to E_F, regardless of magnetic field strength. Therefore, increasing magnetic field leads to a monotonic increase in DOS(E_F) due to the enhanced zeroth LL degeneracy, which further enhances tunneling of electrons of neighboring Bi layers through the Yb-MnBi-Yb barrier when an interlayer electric field is applied. Because 2D Landau quantization in $YbMnBi_2$ is governed by the magnetic field component perpendicular to the Bi plane, such exotic quantum tunneling of the zeroth LL carriers is sensitive to the magnetic field direction and can be detected in angular-dependent magnetotransport such as interlayer MR and the interlayer Hall effect. For example, for the experimental setup shown in **Figure 5*e***, at low field when LLs are not well separated, LL broadening and thermal excitations smear out discrete LLs, which leads to conventional $(\sin\theta)^2$ dependence for the angular-dependent interlayer resistance (AMR) (**Figure 5*f*,** inset). In contrast, when the magnetic field is strong enough to establish the above quantum tunneling scenario, AMR reaches a broad minimum, with θ being approximately 0° due to strong quantum tunneling, but sharply increases for the in-plane field orientation when 2D Landau quantization is suppressed. This causes a surprising strong peak centered at $\theta = 90°$ in AMR, which can be well fitted by the model that includes tunneling of the zeroth LL's carriers (**Figure 5*f***) (270).

3.2.8. Beyond the quantum limit. When magnetic field is strong enough to push all LLs above E_F except for the lowest LL, all electrons are condensed to the lowest LL; such a state is generally referred to as a quantum limit. From this definition, one can find that the critical field needed to reach a quantum limit is at least comparable to the quantum oscillation frequency. The quantum limit is not accessible under a moderate magnetic field for most materials with high carrier density (i.e., large Fermi surface and large quantum oscillation frequency). A system under a quantum limit or an ultraquantum limit may show unusual properties, which has been a long-standing topic of interest even for conventional materials. For instance, a fractional QHE can occur near or in the ultraquantum limit of a 2D electron gas (271). In topological semimetals, the dramatically enhanced degeneracy for the lowest LL, combined with the unique nature of relativistic fermions, may lead to some new exotic phenomena. Indeed, a mass enhancement in the quantum limit has been observed for $ZrTe_5$ (272). This was interpreted as the dynamic mass generation accompanied by density wave formation, which is due to the nesting of the zeroth LL driven by enhanced electron correlation (272). Another example of unusual transport in the quantum limit due to degeneracy enhancement is the aforementioned quantum tunneling of relativistic fermions in $YbMnBi_2$ (247). Because the zeroth LL is pinned at E_F (269), the quantum limit can be reached in relatively low fields in this material (247).

Another phenomenon directly associated with electron condensation to the zeroth LL in topological semimetals is anomalous magnetization (224). The Landau quantization for a 3D WSM yields energy spectra of

$$\varepsilon_{n,k} = \begin{cases} v_F\,\mathrm{sgn}(n)\sqrt{2e\hbar|B||n| + \hbar^2 k_z^2}, & n \neq 0, \\ \chi\,\hbar v_F k_z, & n = 0, \end{cases} \qquad 16.$$

where $\chi = \pm 1$ represents the chirality of the Weyl points. At the quantum limit, magnetization is entirely due to the zeroth LL states, with $M_{n=0} = -\partial\varepsilon_{n=0,k}/\partial B$. Taking the derivatives of Equations 6 and 16, one can find that the magnetization per electron should saturate to a constant in a trivial metal but should vanish in the Weyl case. Therefore, one can expect a collapse of magnetization for topological semimetals crossing the quantum limit. Indeed, the magnetic torque anomaly, which has been observed in NbAs, can be quantitatively described by the topological character of the electronic dispersion (224).

High magnetic field may also lead to annihilation of a Weyl state. The recent studies on TaP have shown that the two counterpropagating chiral modes of the lowest LL (represented by $\chi = \pm 1$ in Equation 16) may hybridize and open up an energy gap, leading to a magnetic tunneling–induced Weyl node annihilation in TaP that manifests as a sharp reversal of the Hall signal (**Figure 6*a***) (273).

In addition to the above phenomena associated with the properties of the relativistic Dirac or Weyl fermions on the zeroth LL, new quantum states in the quantum limit regime have been proposed (274, 275). For $ZrTe_5$, whose carrier density varies with different crystal growth techniques, its quantum limit can be reached under a very small magnetic field (∼0.2 T) for low-carrier-density samples. In the quantum limit, surprising resistivity oscillations periodic in $\log(B)$ have been

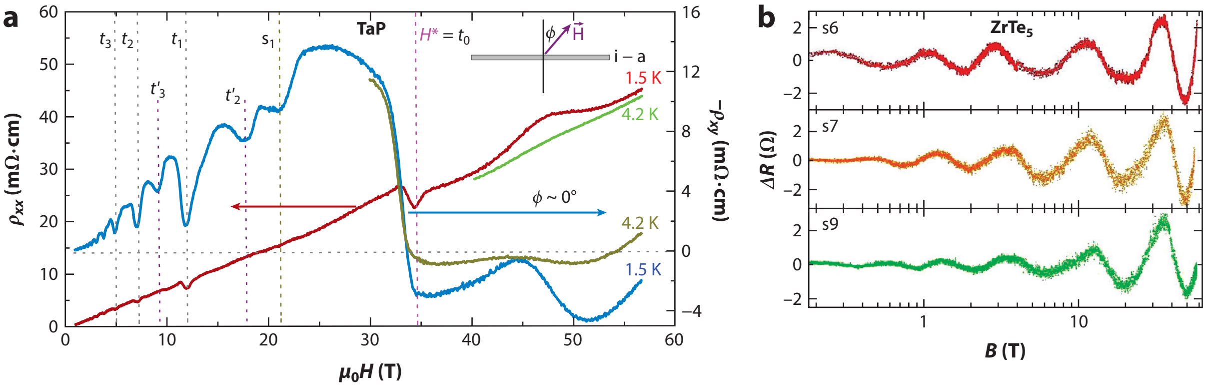

Figure 6

Anomalous transport behavior beyond the quantum limit. (*a*) Magnetic field dependence of the longitudinal (ρ_{xx}) and transverse (ρ_{xy}) resistivity at 1.5 K and 4.2 K for TaP. A steep drop and sign reversal for ρ_{xy} are seen at high field. (*b*) The oscillatory component of resistance ΔR at 4.2 K of three $ZrTe_5$ samples (s6, s7, and s9) with log(B) period. Panel *a* adapted from Reference 273 with permission from Springer Customer Service Centre GmbH, copyright 2017. Panel *b* adapted from Reference 274 under a Creative Commons Attribution 4.0 International License.

observed (**Figure 6*b***) (274), and these oscillations are believed to be associated with the discrete scale invariance and formation of the two-body quasi-bound state (274, 275).

Another long-known but intensively investigated transport behavior in the quantum limit is linear MR. As discussed in Section 3.1, orbital MR stemming from the Lorentz effect should exhibit quadratic or nearly quadratic field dependence. In the quantum limit, however, MR grows linearly with B (195). Such linear MR was discovered in a number of materials (276–280) before the establishment of the theory for topological quantum states. Linear MR has been widely observed in many of the recently reported topological semimetals (45, 172, 173, 175, 234, 235, 281–283). However, linear MR for those materials begins to develop at a field much lower than the critical field needed to reach their quantum limits (45, 172, 173, 175, 234, 235, 281–283). An alternative proposition is that the linear MR in Cd_3As_2 may arise from spatial fluctuations of the magnitude and direction of local current density in disordered systems (172), and this interpretation appears to be applicable for other topological semimetals with linear MR.

3.3. The Intrinsic Anomalous Hall Effect

In Section 3.2, we intensively discuss the phenomena related to the Landau quantization and the zeroth LL in topological semimetals. As indicated above, the unique zeroth LL originates from the Berry phase of the band character of relativistic fermions. In this section, we review another important phenomenon in magnetic topological semimetals, i.e., the intrinsic AHE, which also stems from Berry phase physics.

AHE, the enhanced Hall signal that couples with the magnetization of magnetic materials, has been intensively studied, as discussed in previous reviews (e.g., 284). Generally, the total Hall resistivity ρ_{xy} in a FM material has an anomalous contribution proportional to sample magnetization M ($\rho_{xy}^{AH} = R_s M$) (284). Anomalous Hall resistivity can originate from extrinsic mechanisms such as skew scattering (285) and side jumps (286) and from intrinsic mechanisms due to the topological properties of bands (56, 287–289).

One important feature of magnetic WSMs is their intrinsic AHE. Such an intrinsic Hall component can be understood in terms of the Berry curvature $\vec{\Omega}$ of the electronic Bloch states, which leads to an anomalous electron group velocity perpendicular to the longitudinal electric field $[(e/\hbar)\vec{E} \times \vec{\Omega}]$ (288). In a magnetic WSM, a pair of Weyl nodes with opposite chirality can be seen as monopole sources of Berry curvature. In this case, the AHE is purely intrinsic and tunable by the separation of paired Weyl nodes (54). The intrinsic AHE current is dissipationless (55, 56, 284, 289) and fully spin polarized (289–291) and therefore has great potential for spintronic applications.

A TRS-breaking Weyl state has also been predicted or established in many magnetic compounds. An incomplete list includes Co-based Heusler alloys Co_2XZ (X = IVB or VB; Z = IVA or IIIA) (95–99), half-metallic $Co_3Sn_2S_2$ (93, 94, 292), half-Heusler compounds RPtBi (R = Gd and Nd) with AFM orders (108–110), and the chiral antiferromagnets $MnSn_3$ and $MnGe_3$ (102, 103). The FM Co_2XZ compounds are known to be half-metallic ferromagnets, and some of them have Curie temperatures above room temperature, high spin polarization, and a large Seebeck coefficient (293, 294). It has been theoretically predicted that the locations of the Weyl points of these compounds in momentum space can be tuned by the magnetization direction (96, 97). These properties, together with the predicted giant anomalous Hall conductivity (98, 293), make these materials potentially useful for spintronic and thermoelectric applications. These predictions are awaiting experimental verification. A large intrinsic AHE and a giant anomalous Hall angle were recently reported in FM $Co_3Sn_2S_2$ (94, 292), for which the existence of Weyl fermions has been demonstrated by the observation of surface Fermi arcs (93).

The topological nontrivial states in half-Heusler compounds attracted significant attention even before the discoveries of topological semimetals (108, 295–297). The recent observations of the chiral anomaly—a unique feature of Weyl fermions—together with band structure calculations suggest a magnetic field–driven Weyl state in AFM RPtBi (109, 110). Although different mechanisms such as Zeeman splitting (109) and exchange field (110) have been proposed for the formation of a TRS-breaking Weyl state in these AFM zero-gap semiconductors with quadratic band touching, the intrinsic AHE associated with the magnetic field–driven Weyl state has been probed (**Figure 7*a***), with a very large anomalous Hall angle of ~0.15 comparable to the largest observed in bulk ferromagnets (**Figure 7*b***) (110, 298).

The chiral antiferromagnets Mn_3Sn and Mn_3Ge exhibit large anomalous Hall resistivity in the AFM-ordered state, with a sharp and narrow hysteresis loop in magnetic field sweeps (**Figure 7*c***) (100, 101). In particular, Mn_3Sn is the first antiferromagnet to be discovered to exhibit such a surprising large room temperature AHE (100). Furthermore, remarkable anomalous behavior has also been observed in this material's Nernst effect (57). These anomalous transport features have been ascribed to a magnetic Weyl state, which was subsequently demonstrated both theoretically (102) and experimentally (103).

Although the intrinsic AHE results from magnetic Weyl states, the strong intrinsic AHE does not exclusively occur in magnetic Weyl systems. Other magnetic systems such as FM kagomé metal Fe_2Sn_3 (299), FM spinel $CuCr_2Se_{4-x}Br_x$ (289), and magnetic semiconductors (288, 291) have also been reported to display the intrinsic AHE.

3.4. The Chiral Anomaly

As a hallmark of WSMs, the chiral anomaly is particularly important, as it bridges Weyl fermions in condensed matter physics and in high-energy physics. Generally, the numbers of left- and right-handed Weyl fermions are conserved. This individual conservation of particles with opposite chirality is violated in the presence of parallel electric and magnetic fields. This effect, which was originally proposed in particle physics and termed the Adler–Bell–Jackiw effect or the chiral anomaly (17), leads to exotic transport behaviors in condensed matter, i.e., negative longitudinal MR, AMR narrowing, and the planar Hall effect (PHE), which are discussed in detail below.

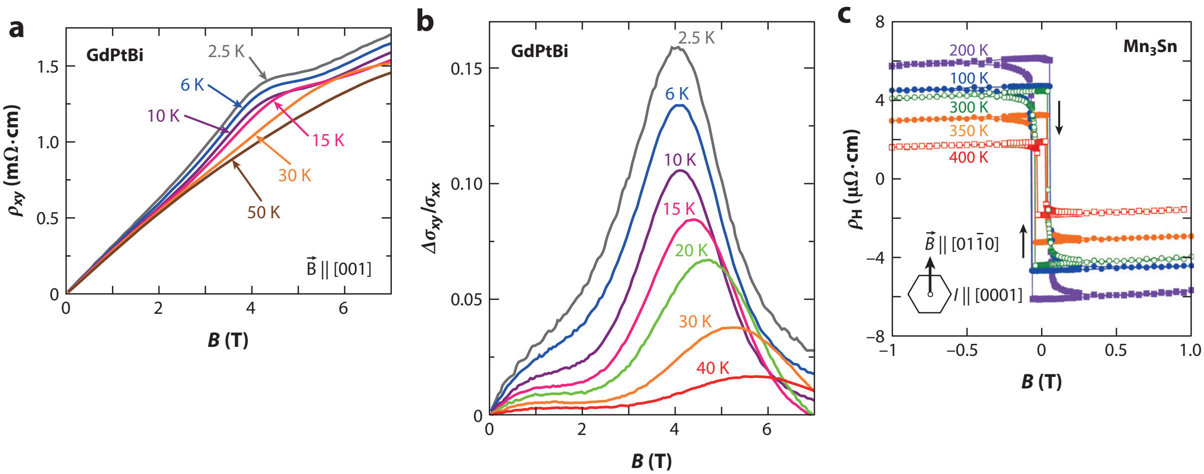

Figure 7

Anomalous Hall effect. (*a*) Magnetic field dependence of the transverse (Hall) resistivity ρ_{xy} for GdPtBi, with field along the [001] direction. (*b*) Anomalous Hall angle $\Delta\sigma_{xy}/\sigma_{xx}$ at different temperatures for GdPtBi. (*c*) Magnetic field dependence of the Hall resistivity ρ_H for Mn_3Sn. Panels *a* and *b* adapted from Reference 298 with permission from Springer Customer Service Centre GmbH, copyright 2016. Panel *c* adapted from Reference 100 with permission from Springer Customer Service Centre GmbH, copyright 2015.

3.4.1. The chiral magnetic effect and negative longitudinal magnetoresistance. Negative longitudinal MR (i.e., the increase in magnetic field parallel to the electrical current leading to a decrease of resistivity) related to the chiral anomaly has been discovered in several topological semimetal systems, as shown below. The chiral anomaly is the manifestation of the chiral magnetic effect: the generation of electric current under magnetic field induced by the chirality imbalance. The mechanism of this phenomenon is well established (10, 11, 52, 53). Here we give a brief overview on its relevant physics. We consider the quantum limit, where only the zeroth LL is occupied. As described in Equation 16 and illustrated in **Figure 8*a***, the 3D Landau quantization of a WSM leads to counterpropagating zeroth LLs for a pair of Weyl cones, which disperse only along the magnetic field direction. This direction is also the direction for electrons to have coherent motion when an external electric field **E** is applied. Such electric field–driven motion leads to electron pumping between Weyl nodes with a rate $\propto -\mathbf{E}\cdot\mathbf{B}$ (10, 11, 53), which results in imbalanced population of carriers between the two zeroth LLs of the paired Weyl cones. As a result, the chirality becomes imbalanced. In condensed matter, this charge pumping process is finally relaxed by inter–Weyl node scattering, and a steady state is reached, with a chiral current $j_c \propto B\mathbf{E}\cdot\mathbf{B}\tau_{\rm int}$, where $\tau_{\rm int}$ is the internode relaxation time (10, 11, 53). Clearly, this chiral current contributes to negative MR when **E//B**. Aside from this quantum mechanical interpretation based on only the zeroth LL, a semiclassical approach based on the Boltzmann equation also yields the same result; with this approach, this formulism can also be generalized to the semiclassical regime that involves multiple LLs (10, 11, 53).

Although the negative longitudinal MR originating from chiral magnetic effect occurs in both the quantum limit and semiclassical regime, the actual field dependence of MR can be material dependent. Generally, the negative MR is expected to be linearly dependent on $\boldsymbol{B}$ in the quantum limit while being $\propto B^2$ in the low-field range. But the real situation can be more complex if the internode scattering that relaxes the chiral charge pumping becomes field dependent. This is possible in the quantum limit at high field, as shown below. In real materials, the situation can be further complicated by positive orbital MR due to the Lorentz effect, which is determined by

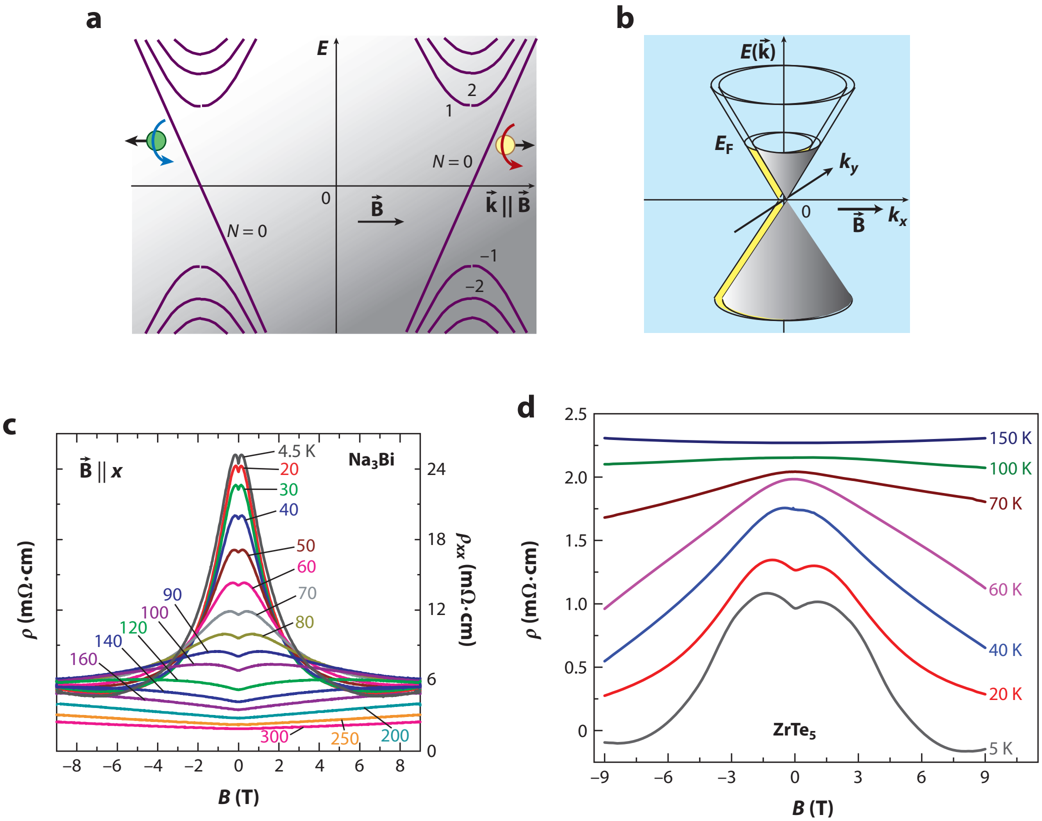

Figure 8

The chiral anomaly and negative longitudinal magnetoresistance (MR). (*a*) Schematic of chiral charge pumping between two Weyl cones with opposite chiralities under parallel magnetic and electric fields. (*b*) Magnetic field–induced Weyl state by lifting the spin degeneracy of a Dirac cone due to the Zeeman effect. (*c*) Longitudinal ρ_{xx} at various temperatures for Na_3Bi. Negative longitudinal MR is observed at lower temperatures. (*d*) Longitudinal ρ_{xx} at various temperatures for $ZrTe_5$. Negative longitudinal MR is observed at lower temperatures. Panels *a*–*c* adapted from Reference 105 with permission from AAAS. Panel *d* adapted from Reference 107 with permission from Springer Customer Service Centre GmbH, copyright 2016.

the magnetic field component perpendicular to current, as discussed in Section 3.1. Ideally, such positive orbital MR should vanish when **E**//**B**, but finite orbital MR may arise from an anisotropic Fermi surface for **E**//**B** (300). Given such orbital effects, the longitudinal MR may show quadratic field dependence in the low-field range but becomes negative when the chiral magnetic effect dominates.

It is also worth noting that the chiral magnetic effect is not limited to the case of exact **E**//**B**, since the chiral charge pumping rate is finite for nonorthogonal electric and magnetic fields. Therefore, negative MR may be observed in a range of field orientation angles and vanishes when it is compensated by the positive orbital MR component, which is determined by the transverse magnetic field component. If the negative MR is too sensitive to field orientation (e.g., it disappears when the magnetic field is deviated by 1° or 2° from the parallel direction), it may suggest a classical origin of current jetting, which is discussed below.

The chiral magnetic effect was first observed in Dirac systems such as $Bi_{0.97}Sb_{0.03}$ (301), Na_3Bi (**Figure 8*c***) (105), Cd_3As_2 (45, 106), and $ZrTe_5$ (**Figure 8*d***) (107) before the experimental discovery of WSMs. This effect can be attributed to the fact that the Dirac point in a 3D DSM can be viewed as a superposition of two paired Weyl nodes with opposite chirality. Such two overlapping Weyl nodes can be separated in momentum space by magnetic field, which breaks TRS (**Figure 8*b***). Half-Heusler *R*PtBi is another group of materials that exhibits the magnetic field–induced chiral magnetic effect (109, 110). As mentioned in Section 3.3, these materials are zero-gap semiconductors, and their Weyl points are believed to be caused by external field–induced Zeeman splitting (109) or by the exchange field from 4*f* electrons (110). It has been proposed that their Weyl points can be induced for any magnetic field orientation and that the induced Weyl points do not necessarily reside on the axis parallel to the field (104). For these field-induced Weyl states, the separation of Weyl points in momentum space may be dependent on magnetic field, so the negative longitudinal MR could display nonuniversal field dependence. For example, a quadratic field dependence of negative MR anticipated for a non–quantum limit regime has been observed for most of the above materials (107, 110, 301). However, a saturation behavior is seen in Na_3Bi (**Figure 8*c***), which is attributed to the field-dependent internode relaxation time in the quantum limit (105).

Since the experimental discoveries of the WSM state in materials such as TaAs class (type I) materials (22, 23, 25, 27, 39, 86–92) and (W/Mo)Te_2 (type II) materials (28, 111–122), many research groups have reported observation of negative longitudinal MR in those materials and have attributed it to the chiral magnetic effect (109, 110, 179–181, 183, 192, 225, 302, 303). Although the chiral anomaly is usually viewed as smoking gun evidence for a Weyl state, one must be cautious before attributing the observed negative longitudinal MR to the chiral anomaly, since a classical effect, current jetting, can also lead to negative longitudinal MR (47). Current jetting is simply due to the rule that the current flows predominately along the high-conductance direction. Once large-conductance anisotropy exists, equipotential lines are strongly distorted, and the current thus forms jets. For materials with large transverse MR, which is the case for most DSMs and WSMs, magnetic field causes very strong conductance anisotropy between the along-current and perpendicular-to-current directions. Therefore, with increasing magnetic field, the voltage drop between voltage contacts may even decrease for asymmetric point–like electrical contacts and irregular sample shape, leading to negative longitudinal MR (10, 304, 305). To minimize such a classical effect, it is important to use a perfect bar-shape sample with a large aspect ratio and well-separated, symmetric voltage contacts. Current jetting is also expected to be weak in materials with small transverse MR [e.g., GdPtBi (304)] due to reduced-conductance anisotropy under magnetic fields. More comprehensive discussions of the current jetting effect in topological semimetals can be found in References 304 and 305.

For type II WSMs such as (W/Mo)Te_2 (28, 111–122), the chiral anomaly shows a different situation. Given the strongly titled Weyl cones in such WSMs, Landau quantization sensitively depends on the orientation of magnetic field, and the Landau spectrum is gapped for some field directions. Therefore, their negative longitudinal MR is strongly anisotropic (28, 306, 307); this has been observed in WTe_2 (302, 303). Further studies also found that, in the classical limit characterized by $\omega_c\tau \ll 1$ (as opposed to the quantum limit or semiclassical limit, where $\omega_c\tau \gg 1$, where ω_c is the cyclotron frequency and τ is the transport relaxation time), negative longitudinal MR in type II WSMs becomes isotropic, similar to that in type I semimetals (303, 308).

3.4.2. The Planar Hall effect. In addition to generating negative MR in longitudinal transport, the chiral anomaly also leads to a nontrivial transverse (Hall) signal under in-plane magnetic field (**Figure 9*a***). Intuitively, an in-plane Hall signal is not expected under in-plane magnetic field due to the absence of electron accumulation on the sample edges. However, in-plane Hall voltage can be generated in the presence of coplanar electric and magnetic fields (**Figure 9*a***) due to the chiral anomaly, leading to the so-called PHE (309–315).

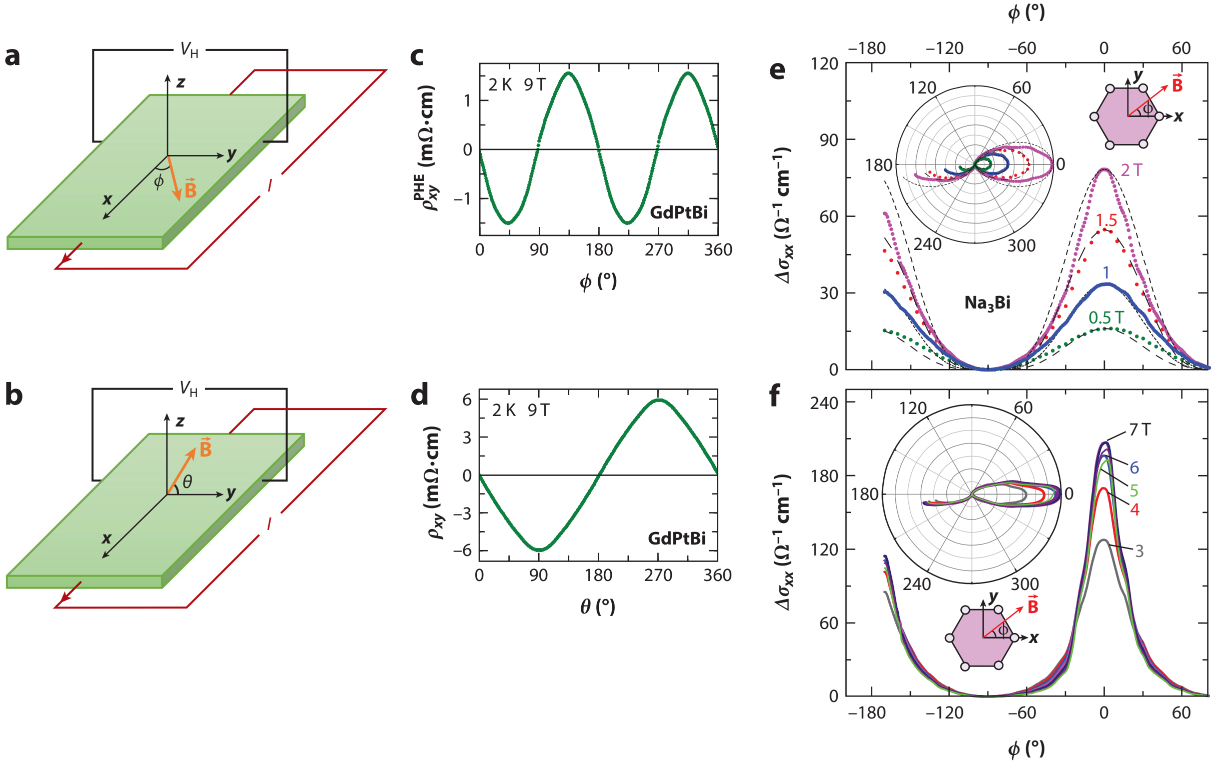

Figure 9

The planar Hall effect (PHE) and angular-dependent interlayer resistance narrowing. (*a*) Experimental setup for the PHE. The magnetic field is rotated within the sample plane (the *x*-*y* plane). (*b*) Experimental setup for the conventional Hall effect. The magnetic field is rotated from the out-of-plane direction toward the sample plane (the *y*-*z* plane). (*c*,*d*) Angular dependence of (*c*) planar (ρ_{xy}^{PHE}) and (*d*) conventional (ρ_{xy}) Hall resistivity in GdPtBi at 9 T and 2 K, using the setup shown in panels *a* and *b*, respectively. A twofold symmetry is observed for the PHE, in contrast with a onefold symmetry for the conventional Hall effect. (*e*,*f*) Magnetic field orientation dependence of the magnetoconductivity [$\Delta\sigma_{xx} = \sigma_{xx}(B,\phi) - \sigma_{xx}(B,90°)$] of Na_3Bi at 4.5 K, measured at (*e*) low and (*f*) high magnetic fields. The insets show the same data in polar representation. The peak profiles in the angular dependence are clearly narrower at high fields. Panels *c* and *d* adapted with permission from Reference 313. Copyright 2018, American Physical Society. Panels *e* and *f* adapted from Reference 105 with permission from AAAS.

The PHE, a well-known phenomenon observed in ferromagnets, is due to the resistivity anisotropy caused by anisotropic magnetization (316). Although topological semimetals have the same in-plane angular dependence in Hall resistivity ρ_{xy} as do ferromagnets, the PHE in topological semimetals occurs in the absence of magnetic order, with a significantly enhanced amplitude (309, 310). With coplanar electric and magnetic fields, the transverse resistance ρ_{xy} of the PHE is (309)

$$\rho_{xy} = \frac{(\rho_{||} - \rho_{\perp})}{2} \sin 2\varphi, \qquad 17.$$

where $\rho_{||}$ and $\rho_{\perp}$ denote resistivity with current flowing along and perpendicular to the direction of the magnetic field, respectively, and φ is the angle between the current flow and magnetic field orientation (**Figure 9*a***). As discussed in Section 3.2, in the Drude model, the orbital MR for *B*//*I* is strictly zero unless a multiband effect is involved. Therefore, $\rho_{||} - \rho_{\perp}$ represents the resistivity anisotropy caused by the chiral anomaly.

In experimental studies on DSMs and WSMs, an abnormal Hall signal under in-plane magnetic field was first reported in $ZrTe_5$ (317). A strict $\sin 2\varphi$ dependence was later observed in a number of materials, including $ZrTe_5$, Cd3As_2, GdPtBi, WTe_2, and VAl_3 (311–315). With rotating in-plane field (**Figure 9*a***) and out-of-plane field (**Figure 9*b***), the twofold anisotropy of the PHE (**Figure 9*c***) clearly differs from the onefold symmetry seen for the conventional Hall effect (**Figure 9*d***) (313). Unlike the conventional Hall effect, the PHE does not satisfy antisymmetry; i.e., $\rho_{xy} \neq -\rho_{yx}$. This is because the PHE does not originate from the Lorentz force (309, 310).

3.4.3. Narrowing of angular-dependent interlayer resistance.

With the above definition of $\rho_{\parallel}$ and $\rho_{\perp}$, longitudinal resistivity can be expressed as (309)

$$\rho_{xx} = \rho_{\perp} + (\rho_{\parallel} - \rho_{\perp})\cos^2 \varphi. \qquad 18.$$

Another unusual property that can be derived from Equation 18 is the narrowing of the AMR peak at high magnetic field (309). For simplicity, magnetoconductivity with sweeping in-plane angle φ may be expressed as $\frac{1}{\rho_{xx}(B,\varphi)} - \frac{1}{\rho_{xx}(0,\varphi)}$ (a stricter process requires tensor conversion). At a small angle, the angular dependence of magnetoconductivity has a Lorentzian profile with angular width (309):

$$\Delta\varphi \approx \left(\frac{\varepsilon_{\mathrm{F}}}{\hbar v_{\mathrm{F}}/l_{\mathrm{B}}}\right)^2 \sqrt{\frac{\tau}{\tau_{\mathrm{c}}}}, \qquad 19.$$

where $l_{\mathrm{B}} = \sqrt{\hbar/eB}$ is the magnetic length, τ_{c} is the relaxation time for chiral charge diffusion, and τ is the conventional momentum relaxation time. At low fields, LLs are wiped out by energy level broadening and thermal excitation. In this case, the parameters involved in Equation 19 are field independent except for l_{B}, indicating a narrowing of angular width with B that has been observed in Na_3Bi (**Figure 8*e,f***) (176). When a strong magnetic field drives the system to the quantum limit, the field dependence of each parameter in Equation 19 leads to the saturation of $\Delta\varphi$, as shown in **Figure 9*e,f*** (176).

3.5. Quantum Hall States in the 2D Limit

Topological semimetal phases may evolve into new topological quantum states in low dimensions.

3.5.1. Classifications of the various quantum Hall states.

In the 2D limit, one intriguing aspect of topological semimetals is the potential to generate various quantum Hall states. In Section 3.2.8, we mention that the QHE in the 3D layered topological semimetal $EuMnBi_2$ is caused by the formation of 2D electronic states due to restriction of electron motion in the 2D Bi plane (177). Here we discuss two other quantum Hall states in the 2D limit that have potential applications in electronics and spintronics: the QSHI (i.e., 2D topological insulator) state and the QAHI state.

The 2D quantum Hall states for both nonrelativistic and relativistic electrons reflect the fundamental topological properties of materials. For example, the integer QHE, an established phenomenon that was well understood in terms of Landau quantization, now has a topological interpretation based on the topological invariant of the Chern number, which opens up the field of topological electronic states in condensed matter. As shown in **Figure 10*a*** and mentioned in Section 3.2.7, an integer quantum Hall system under sufficiently strong fields is characterized by an insulating bulk state with electrons pinned to quantized small radii orbits and a conducting, dissipationless chiral edge state formed by skipping orbits. The superposition of two copies of

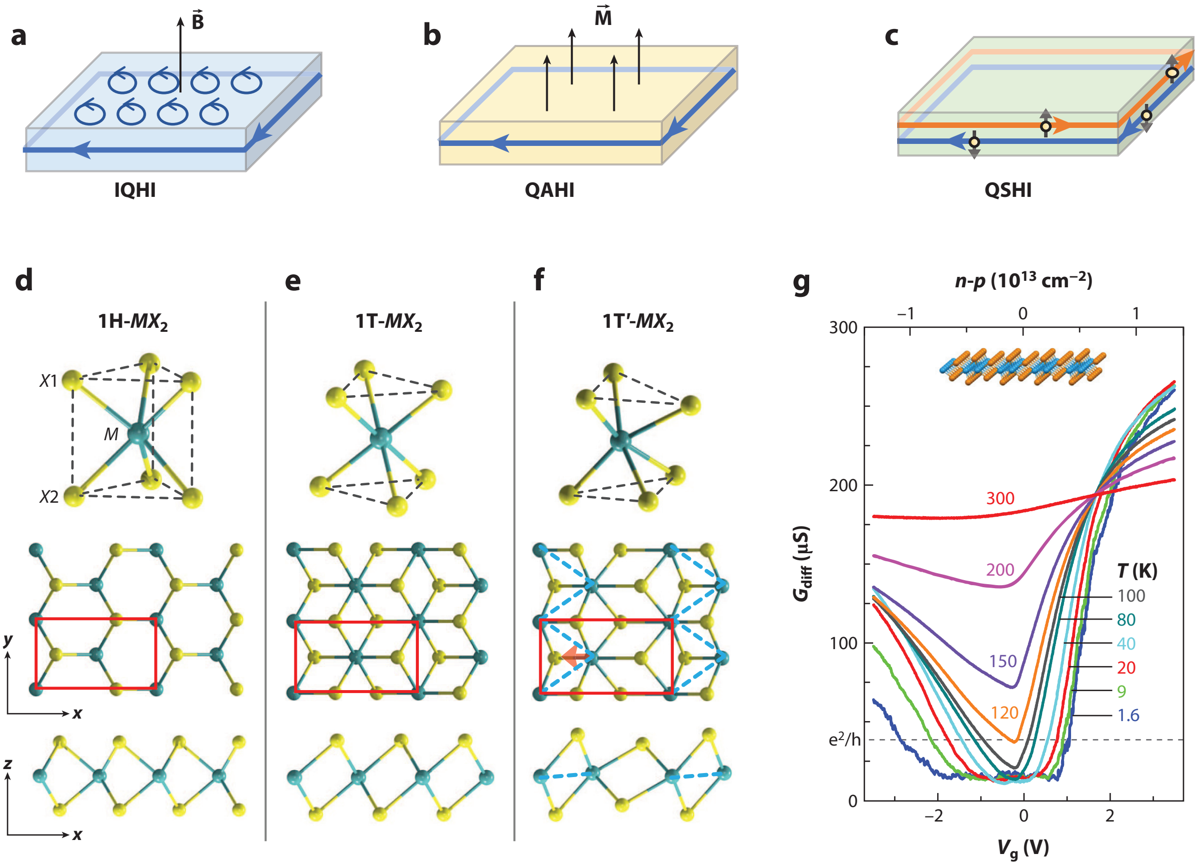

Figure 10

Quantum Hall effects in various topological phases. (*a–c*) Schematic for (*a*) the integer quantum Hall insulator (IQHI) state, (*b*) the quantum anomalous Hall insulator (QAHI) state, and (*c*) the quantum spin Hall insulator (QSHI) state. (*d–f*) The (*d*) 1H, (*e*) 1T, and (*f*) 1T′ structures of monolayer transition metal dichalcogenides. Panels *d–f* adapted from Reference 72 with permission from AAAS. (*g*) Gate voltage dependence of the differential conductance of the monolayer WTe_2 at difference temperatures. Panel *g* adapted from Reference 74 with permission from Springer Customer Service Centre GmbH, copyright 2017.

time-reversal integer quantum Hall systems in the quantum limit leads to the QSHI, i.e., the 2D topological insulator, which displays a pair of counterpropagating, spin-polarized edge states due to spin-orbit locking (**Figure 10*c***). Apparently, the magnetic field necessary to produce an integer quantum Hall system is no longer needed for a QSHI system (76, 79), as the magnetic field is cancelled out when the time-reversal copies of integer quantum Hall systems are brought together. Another modification of the integer quantum Hall system that does not require an external magnetic field is the QAHI state, in which spontaneous magnetization leads to the dissipationless chiral edge state (**Figure 10*b***) and the formation of LLs is not required (76, 79).

The QSHI and QAHI states also provide significant insights into topological physics beyond simple modification of the integer quantum Hall system (76). The QAHI and the integer quantum Hall system are essentially 2D Chern insulators characterized by nonzero Chern numbers, in contrast with a trivial insulator with $C = 0$. With TRS, the Chern number must vanish, but another topological invariant, the Z_2 number, can be introduced to clarify the 2D insulators, becoming 0 for trivial insulators and 1 for a symmetry-protected topological insulator (QSHI) (318). Simple stacking of these 2D building blocks leads to a 3D weak Chern insulator or a weak topological insulator that is not robust against disorder (319). It is also possible to extend the topological classification of a QSHI to 3D and create a strong 3D topological insulator (319). However, the extension of the 2D Chern insulator to 3D cannot produce a strong 3D Chern insulator. Instead, this development results in a metallic phase: the topological semimetal (76). The above discussions show how quantum Hall systems, QSHIs, QAHIs, 3D topological insulators, and topological semimetals are closely connected in terms of the topological properties, which implies the possibility of conversion between these states.

From the experimental aspect, QSHIs and QAHIs are expected to display unusual nonlocal transport (320, 321). The resistance or conductance of conventional diffusive systems is dependent on the dimensions of the sample and is determined by the local resistivity or conductivity (Ohm's law). However, in quantum Hall systems, due to scale-invariant dissipationless edge conduction, transport is nonlocal, and the concepts of resistivity or conductivity are thus meaningless. The Hall conductance can be obtained from the Chern number C by $G_{xy} = Ce^2/h$; a half-quantized Hall conductance is also expected for massless relativistic fermions, as discussed in Section 3.2.8 (Equation 15). For a QSHI, $G_{xy} = 0$ due to $C = 0$ in a TRS system, which can be attributed to the fact that the pair of time-reversed chiral edge states cancels each other (**Figure 10*c***). For the longitudinal conductance G_{xx}, the measurement results strongly depend on the configuration of the contact electrodes. This is because an ideal contact attached to the edge of the sample acts as a reservoir that draws electrons and emits them from and to the edge channels. The spin information of an electron is smeared out during this process. For an integer quantum Hall system or a QAHI system, the edge state is chiral (**Figure 10*a*,*b***), and the electrons emitted from the contact have to flow along the same direction, which should lead to zero longitudinal conductance and hence zero longitudinal resistance according to resistivity and conductivity tensor conversion. However, for a QSHI with time-reversed spin-polarized edge states, the spin of the emitted electrons has half probability to be reversed, corresponding to the back-moving edge channel with opposite spin. Therefore, a finite resistance depending on the number and configuration of contacts can be expected (320, 321).

3.5.2. Material realizations for the QSHI and QAHI states. The QSHI state has been proposed in the monolayer form of the layered 1T′–transition metal dichalcogenides MX_2 (M = W, Mo; X = S, Se, Te) (72) and WHM (322). The structure of monolayer MX_2 is formed from the stacking of X-M-X layers, with its physical properties being determined by the type of stacking. A hexagonal H structure with ABA stacking (**Figure 10*d***) results in the well-known direct-band-gap semiconductors (323). For a rhombohedral 1T phase with ABC stacking (**Figure 10*e***), the structure is unstable and undergoes a spontaneous lattice distortion to the 1T′ phase (**Figure 10*f***), which consequently leads to a QSHI state in the presence of SOC (72). The QSHI state in monolayer 1T′-MX_2 was first demonstrated in WTe_2, as this material naturally has the 1T′ structure in the bulk form. There is transport (74, 75) and spectroscopic (73) evidence of the QSHI state in WTe_2 monolayers prepared using mechanical exfoliation or molecular beam epitaxy (MBE) growth. For example, upon sweeping the gate voltage, a conductance plateau associated with the 1D edge state of a QSHI is observed in a WTe_2 monolayer (**Figure 10*g***) but is absent in bilayer or few-layer samples (74, 75). More importantly, the temperature at which the conductance plateau starts to develop is as high as 100 K (**Figure 10*g***), which is greatly higher than the operating temperature of other well-established QSHIs in semiconductor quantum wells (324) and could be ascribed to the large bulk band gap of the 1T′-WTe_2 monolayer [which was predicted to be 100 meV (72) and found to be 55 ± 20 meV for MBE-grown samples (73)]. This finding has great potential for practical device applications. Furthermore, under one proposal, the horizontal electric field may break the inversion symmetry and may induce strong Rashba splitting of the bands near E_F, which closes the bulk gap at some critical electric fields. Such gap closing leads to a topological phase transition to a trivial phase; this transition occurs very rapidly and can thus be used for topological field effect transistors (72).

The tetragonal layered *WHM* compounds have also been predicted to become QSHIs in the monolayer form (322). Different from WTe_2, which is a type II topological WSM in the bulk form (28, 111–113, 117), bulk *WHM* is predicted to be a weak topological insulator formed from the stacking of QSHIs (322, 325); this is a long-sought topological quantum state (326). In *WHM*, C_{2v} symmetry ensures nodal-line crossings near E_F in the absence of SOC, but this symmetry cannot prevent SOC gap opening (154). Because the Fermi level crosses the gapped cones and the band dispersion is extremely linear over a wide energy range, *WHM*s have been established as topological NLSMs (78, 85, 154). To realize the predicted QSHI state, one possible route is to exfoliate the bulk *WHM*s to their monolayers. Although the interlayer coupling in *WHM*s is not van der Waals type (322, 327), the weak coupling strength in some *WHM*s allows for mechanical exfoliation, as has been demonstrated (156). One possible advantage of using *WHM*s as a platform for realizing QSHIs is the variable SOC gap with various combinations of *W*, *H*, and *M* (226); such a gap offers the opportunity to design different QSHIs.

As mentioned above, a QAHI system is in principle similar to the integer quantum Hall system, but the former occurs without an external magnetic field and LLs (76, 79) and thus carries great promise for possible applications in spintronics. Furthermore, a QAHI system also provides a promising platform for the creation, manipulation, and utilization of Majorana fermions, the hypothetical particles that are their own antiparticles (328, 329). The QAHI state was first experimentally demonstrated in magnetically doped topological insulators (330–332). However, it has so far been realized only at very low temperatures (<1 K) (330–332). Room temperature QAHIs, if realized, will have the potential to revolutionize information technology through dissipationless spin-polarized chiral edge transport in spintronic devices. Recent studies have revealed a new possible route to the realization of high-temperature QAHIs: 3D FM WSMs can evolve into large-gap QAHIs when the dimensionality is reduced from 3D to 2D, due to the confinement-induced quantization of low-energy states (21). One possible candidate material is $HgCr_2Se_4$ (21), which is awaiting experimental verification. In addition to these two approaches, there are other proposals for the realization of QAHIs (76).

4. SUMMARY AND PERSPECTIVE

Above we review distinct electronic transport phenomena associated with nontrivial band topology in different types of topological semimetals and discuss how to extract the fundamental properties of Dirac/Weyl fermions such as effective mass, quantum mobility, and the Berry phase from dHvA or SdH quantum oscillation measurements. The above discussion shows that topological semimetals exhibit a rich variety of exotic properties that are not seen in nonrelativistic electron systems. These properties include the chiral anomaly and the PHE in WSMs, the intrinsic AHE in TRS-breaking WSMs, quantum oscillations due to Weyl orbits and AMR peak narrowing under high magnetic fields in DSMs, the half-integer QHE and quantum tunneling of the zeroth LLs in layered magnetic DSMs, and vanishing magnetization and dynamic mass generation in the quantum limit of DSMs/WSMs. We discuss how these properties are connected with nontrivial band topology, although the mechanisms for some of these properties are not fully understood. Furthermore, we discuss how DSMs/WSMs are linked with the QSHI and QAHI states and how these two quantum Hall states can be approached by reducing NLSMs/FM WSMs to 2D thin layers.

As previous reviews have noted (10, 11), one challenge in this field is the experimental realization of ideal model systems like graphene (10) or the hydrogen atom (11) for various types of topological semimetal phases. An ideal model system should contain only the topological band(s), with the same types of Dirac or Weyl points being symmetrically related, located at the Fermi energy level, and well separated in momentum space. For the material aspect, such a system should be stable in the ambient environment and have minimal defects (10, 11). As noted above, the topological semimetals discovered so far are probably the tip of the iceberg. Given that topological semimetals can be predicted by band structure calculations, we believe that many new topological semimetal phases and candidate materials will be discovered and that some of them may serve as model systems. There have been recent breakthroughs in topological phase screening and database development for topological quantum materials (37, 325, 333–336a). With new simple model systems, the trivial bands will not mask or interfere with the contributions from exotic phenomena arising from the nontrivial bands, and novel knowledge of various topological semimetal phases can be further revealed.

Topological quantum materials have stimulated great interest because of not only their connection with high-energy particle physics but also their great potential in future technology applications. As discussed above, both the QSHI and QAHI states can be obtained by reducing the dimension of NLSMs/FM WSMs to 2D, and these two states can support dissipationless transport through their topological spin-polarized edge states. Therefore, they carry great promise for applications for spintronic devices and quantum computation. Although both the QSHIs and QAHIs have been demonstrated experimentally, these states currently occur only in the low-temperature range. Pushing their operation temperature to room temperature is another great challenge in the field. Achieving this goal requires discoveries of new topological materials with better properties, along with integrated efforts in theoretical modeling, computation, synthesis, characterization, and device demonstrations.

DISCLOSURE STATEMENT

The authors are not aware of any affiliations, memberships, funding, or financial holdings that might be perceived as affecting the objectivity of this review.

ACKNOWLEDGMENTS

J.H. is supported by the US Department of Energy (DOE), Office of Science, Basic Energy Sciences program under award DE-SC0019467. Z.M. is supported by the US National Science Foundation under grant DMR1707502. N.N. is supported by the US DOE, Office of Science, Basic Energy Sciences program under award DE-SC0011978. We thank Prof. Antony Carrington from Bristol University for informative discussions on the effective mass for multifrequency oscillations.

LITERATURE CITED

1. Wilczek F. 1998. Why are there analogies between condensed matter and particle theory? *Phys. Today* 51:11
2. Volovik GE. 2009. *The Universe in a Helium Droplet*. Oxford, UK: Oxford Univ. Press
3. Geim AK, Novoselov KS. 2007. The rise of graphene. *Nat. Mater.* 6:183–91
4. Hasan MZ, Kane CL. 2010. Topological insulators. *Rev. Mod. Phys.* 82:3045–67
5. Qi X-L, Zhang S-C. 2011. Topological insulators and superconductors. *Rev. Mod. Phys.* 83:1057–110

6. Vafek O, Vishwanath A. 2014. Dirac fermions in solids: from high-T_c cuprates and graphene to topological insulators and Weyl semimetals. *Annu. Rev. Condens. Matter Phys.* 5:83–112
7. Jia S, Xu S-Y, Hasan MZ. 2016. Weyl semimetals, Fermi arcs and chiral anomalies. *Nat. Mater*. 15:1140–44
8. Yan B, Felser C. 2017. Topological materials: Weyl semimetals. *Annu. Rev. Condens. Matter Phys.* 8:337–54
9. Burkov AA. 2018. Weyl metals. *Annu. Rev. Condens. Matter Phys.* 9:359–78
10. Armitage NP, Mele EJ, Vishwanath A. 2018. Weyl and Dirac semimetals in three-dimensional solids. *Rev. Mod. Phys*. 90:015001
11. Bernevig A, Weng H, Fang Z, Dai X. 2018. Recent progress in the study of topological semimetals. *J. Phys. Soc. Jpn.* 87:041001
12. Young SM, Zaheer S, Teo JCY, Kane CL, Mele EJ, Rappe AM. 2012. Dirac semimetal in three dimensions. *Phys. Rev. Lett*. 108:140405
13. Wang Z, Sun Y, Chen X-Q, Franchini C, Xu G, et al. 2012. Dirac semimetal and topological phase transitions in A_3Bi (A = Na, K, Rb). *Phys. Rev. B* 85:195320
14. Wang Z, Weng H, Wu Q, Dai X, Fang Z. 2013. Three-dimensional Dirac semimetal and quantum transport in Cd_3As_2. *Phys. Rev. B* 88:125427
15. Weyl H. 1929. Elektron und Gravitation. I. *Z. Phys.* 56:330–52
16. Herring C. 1937. Accidental degeneracy in the energy bands of crystals. *Phys. Rev.* 52:365–73
17. Nielsen HB, Ninomiya M. 1983. The Adler-Bell-Jackiw anomaly and Weyl fermions in a crystal. *Phys. Lett. B* 130:389–96
18. Abrikosov AA, Beneslavskii SD. 1971. Some properties of gapless semiconductors of the second kind. *J. Low Temp. Phys.* 5:141–54
19. Wan X, Turner AM, Vishwanath A, Savrasov SY. 2011. Topological semimetal and Fermi-arc surface states in the electronic structure of pyrochlore iridates. *Phys. Rev. B* 83:205101
20. Burkov AA, Balents L. 2011. Weyl semimetal in a topological insulator multilayer. *Phys. Rev. Lett.* 107:127205
21. Xu G, Weng H, Wang Z, Dai X, Fang Z. 2011. Chern semimetal and the quantized anomalous Hall effect in $HgCr_2Se_4$. *Phys. Rev. Lett.* 107:186806
22. Huang S-M, Xu S-Y, Belopolski I, Lee C-C, Chang G, et al. 2015. A Weyl fermion semimetal with surface Fermi arcs in the transition metal monopnictide TaAs class. *Nat. Commun*. 6:7373
23. Weng H, Fang C, Fang Z, Bernevig BA, Dai X. 2015. Weyl semimetal phase in noncentrosymmetric transition-metal monophosphides. *Phys. Rev. X* 5:011029
24. Dirac PAM. 1928. The quantum theory of the electron. *Proc. R. Soc. A* 117:610–24
25. Xu S-Y, Belopolski I, Alidoust N, Neupane M, Bian G, et al. 2015. Discovery of a Weyl fermion semimetal and topological Fermi arcs. *Science* 349:613–17
26. Lu L, Wang Z, Ye D, Ran L, Fu L, et al. 2015. Experimental observation of Weyl points. *Science* 349:622–24
27. Lv BQ, Weng HM, Fu BB, Wang XP, Miao H, et al. 2015. Experimental discovery of Weyl semimetal TaAs. *Phys. Rev. X* 5:031013
28. Soluyanov AA, Gresch D, Wang Z, Wu Q, Troyer M, et al. 2015. Type-II Weyl semimetals. *Nature* 527:495–98
29. Chang T-R, Xu S-Y, Sanchez DS, Tsai W-F, Huang S-M, et al. 2017. Type-II symmetry-protected topological Dirac semimetals. *Phys. Rev. Lett.* 119:026404
30. Burkov AA, Hook MD, Balents L. 2011. Topological nodal semimetals. *Phys. Rev. B* 84:235126
31. Bradlyn B, Cano J, Wang Z, Vergniory MG, Felser C, et al. 2016. Beyond Dirac and Weyl fermions: unconventional quasiparticles in conventional crystals. *Science* 353:aaf5037
32. Wieder BJ, Kim Y, Rappe AM, Kane CL. 2016. Double Dirac semimetals in three dimensions. *Phys. Rev. Lett.* 116:186402
33. Weng H, Fang C, Fang Z, Dai X. 2016. Topological semimetals with triply degenerate nodal points in q-phase tantalum nitride. *Phys. Rev. B* 93:241202
34. Zhu Z, Winkler GW, Wu Q, Li J, Soluyanov AA. 2016. Triple point topological metals. *Phys. Rev. X* 6:031003

35. Weng H, Fang C, Fang Z, Dai X. 2016. Coexistence of Weyl fermion and massless triply degenerate nodal points. *Phys. Rev. B* 94:165201
36. Chang G, Xu S-Y, Huang S-M, Sanchez DS, Hsu C-H, et al. 2017. Nexus fermions in topological symmorphic crystalline metals. *Sci. Rep.* 7:1688
37. Watanabe H, Po HC, Vishwanath A. 2018. Structure and topology of band structures in the 1651 magnetic space groups. *Sci. Adv.* 4:eaat8685
38. Xu S-Y, Liu C, Kushwaha SK, Sankar R, Krizan JW, et al. 2015. Observation of Fermi arc surface states in a topological metal. *Science* 347:294–98
39. Yang LX, Liu ZK, Sun Y, Peng H, Yang HF, et al. 2015. Weyl semimetal phase in the noncentrosymmetric compound TaAs. *Nat. Phys.* 11:728–32
40. Bian G, Chang T-R, Sankar R, Xu S-Y, Zheng H, et al. 2016. Topological nodal-line fermions in spin-orbit metal $PbTaSe_2$. *Nat. Commun.* 7:10556
41. Inoue H, Gyenis A, Wang Z, Li J, Oh SW, et al. 2016. Quasiparticle interference of the Fermi arcs and surface-bulk connectivity of a Weyl semimetal. *Science* 351:1184–87
42. Batabyal R, Morali N, Avraham N, Sun Y, Schmidt M, et al. 2016. Visualizing weakly bound surface Fermi arcs and their correspondence to bulk Weyl fermions. *Sci. Adv.* 2:e1600709
43. Potter AC, Kimchi I, Vishwanath A. 2014. Quantum oscillations from surface Fermi arcs in Weyl and Dirac semimetals. *Nat. Commun.* 5:5161
44. Moll PJW, Nair NL, Helm T, Potter AC, Kimchi I, et al. 2016. Transport evidence for Fermi-arc-mediated chirality transfer in the Dirac semimetal Cd_3As_2. *Nature* 535:266–70
45. Liang T, Gibson Q, Ali MN, Liu M, Cava RJ, Ong NP. 2015. Ultrahigh mobility and giant magnetoresistance in the Dirac semimetal Cd_3As_2. *Nat. Mater.* 14:280–84
46. Shekhar C, Nayak AK, Sun Y, Schmidt M, Nicklas M, et al. 2015. Extremely large magnetoresistance and ultrahigh mobility in the topological Weyl semimetal candidate NbP. *Nat. Phys.* 11:645–49
47. Pippard AB. 1989. *Magnetoresistance in Metals*. Cambridge, UK: Cambridge Univ. Press
48. Ali MN, Xiong J, Flynn S, Tao J, Gibson QD, et al. 2014. Large, non-saturating magnetoresistance in WTe_2. *Nature* 514:205–8
49. Skinner B, Fu L. 2018. Large, nonsaturating thermopower in a quantizing magnetic field. *Sci. Adv.* 4:eaat2621
50. Liang T, Gibson Q, Xiong J, Hirschberger M, Koduvayur SP, et al. 2013. Evidence for massive bulk Dirac fermions in $Pb_{1-x}Sn_xSe$ from Nernst and thermopower experiments. *Nat. Commun.* 4:2696
51. Stockert U, dos Reis RD, Ajeesh MO, Watzman SJ, Schmidt M, et al. 2017. Thermopower and thermal conductivity in the Weyl semimetal NbP. *J. Phys. Condens. Matter* 29:325701
52. Jho Y-S, Kim K-S. 2013. Interplay between interaction and chiral anomaly: anisotropy in the electrical resistivity of interacting Weyl metals. *Phys. Rev. B* 87:205133
53. Son DT, Spivak BZ. 2013. Chiral anomaly and classical negative magnetoresistance of Weyl metals. *Phys. Rev. B* 88:104412
54. Burkov AA. 2014. Anomalous Hall effect in Weyl metals. *Phys. Rev. Lett.* 113:187202
55. Karplus R, Luttinger JM. 1954. Hall effect in ferromagnetics. *Phys. Rev.* 95:1154–60
56. Haldane FDM. 2004. Berry curvature on the Fermi surface: anomalous Hall effect as a topological Fermi-liquid property. *Phys. Rev. Lett.* 93:206602
57. Ikhlas M, Tomita T, Koretsune T, Suzuki M-T, Nishio-Hamane D, et al. 2017. Large anomalous Nernst effect at room temperature in a chiral antiferromagnet. *Nat. Phys.* 13:1085–90
58. Sakai A, Mizuta YP, Nugroho AA, Sihombing R, Koretsune T, et al. 2018. Giant anomalous Nernst effect and quantum-critical scaling in a ferromagnetic semimetal. *Nat. Phys.* 14:1119–24
59. Ishizuka H, Hayata T, Ueda M, Nagaosa N. 2016. Emergent electromagnetic induction and adiabatic charge pumping in noncentrosymmetric Weyl semimetals. *Phys. Rev. Lett.* 117:216601
60. Taguchi K, Imaeda T, Sato M, Tanaka Y. 2016. Photovoltaic chiral magnetic effect in Weyl semimetals. *Phys. Rev. B* 93:201202
61. Chan C-K, Lindner NH, Refael G, Lee PA. 2017. Photocurrents in Weyl semimetals. *Phys. Rev. B* 95:041104

62. de Juan F, Grushin AG, Morimoto T, Moore JE. 2017. Quantized circular photogalvanic effect in Weyl semimetals. *Nat. Commun.* 8:15995
63. Ma Q, Xu S-Y, Chan C-K, Zhang C-L, Chang G, et al. 2017. Direct optical detection of Weyl fermion chirality in a topological semimetal. *Nat. Phys.* 13:842–47
64. Osterhoudt GB, Diebel LK, Gray MJ, Yang X, Stanco J, et al. 2019. Colossal mid-infrared bulk photovoltaic effect in a type-I Weyl semimetal. *Nat. Mater*. 18:471–75
65. Wu L, Patankar S, Morimoto T, Nair NL, Thewalt E, et al. 2016. Giant anisotropic nonlinear optical response in transition metal monopnictide Weyl semimetals. *Nat. Phys.* 13:350–55
66. Morimoto T, Nagaosa N. 2016. Topological nature of nonlinear optical effects in solids. *Sci. Adv.* 2:e1501524
67. Goswami P, Sharma G, Tewari S. 2015. Optical activity as a test for dynamic chiral magnetic effect of Weyl semimetals. *Phys. Rev. B* 92:161110
68. Ma J, Pesin DA. 2015. Chiral magnetic effect and natural optical activity in metals with or without Weyl points. *Phys. Rev. B* 92:235205
69. Zhong S, Moore JE, Souza I. 2016. Gyrotropic magnetic effect and the magnetic moment on the Fermi surface. *Phys. Rev. Lett.* 116:077201
70. Feng W, Guo G-Y, Zhou J, Yao Y, Niu Q. 2015. Large magneto-optical Kerr effect in noncollinear antiferromagnets Mn_3X (X = Rh, Ir, Pt). *Phys. Rev. B* 92:144426
71. Higo T, Man H, Gopman DB, Wu L, Koretsune T, et al. 2018. Large magneto-optical Kerr effect and imaging of magnetic octupole domains in an antiferromagnetic metal. *Nat. Photon.* 12:73–78
72. Qian X, Liu J, Fu L, Li J. 2014. Quantum spin Hall effect in two-dimensional transition metal dichalcogenides. *Science* 346:1344–47
73. Tang S, Zhang C, Wong D, Pedramrazi Z, Tsai H-Z, et al. 2017. Quantum spin Hall state in monolayer 1T′-WTe_2. *Nat. Phys.* 13:683–87
74. Fei Z, Palomaki T, Wu S, Zhao W, Cai X, et al. 2017. Edge conduction in monolayer WTe_2. *Nat. Phys.* 13:677–82
75. Wu S, Fatemi V, Gibson QD, Watanabe K, Taniguchi T, et al. 2018. Observation of the quantum spin Hall effect up to 100 Kelvin in a monolayer crystal. *Science* 359:76–79
76. Weng H, Yu R, Hu X, Dai X, Fang Z. 2015. Quantum anomalous Hall effect and related topological electronic states. *Adv. Phys.* 64:227–82
77. Burkov AA. 2015. Chiral anomaly and transport in Weyl metals. *J. Phys. Condens. Matter* 27:113201
78. Chen F, Hongming W, Xi D, Zhong F. 2016. Topological nodal line semimetals. *Chin. Phys. B* 25:117106
79. Liu C-X, Zhang S-C, Qi X-L. 2016. The quantum anomalous Hall effect: theory and experiment. *Annu. Rev. Condens. Matter Phys.* 7:301–21
80. Bansil A, Lin H, Das T. 2016. Topological band theory. *Rev. Mod. Phys.* 88:021004
81. Wang S, Lin B-C, Wang A-Q, Yu D-P, Liao Z-M. 2017. Quantum transport in Dirac and Weyl semimetals: a review. *Adv. Phys. X* 2:518–44
82. Hasan MZ, Xu S-Y, Belopolski I, Huang S-M. 2017. Discovery of Weyl fermion semimetals and topological Fermi arc states. *Annu. Rev. Condens. Matter Phys.* 8:289–309
83. Zheng H, Zahid Hasan M. 2018. Quasiparticle interference on type-I and type-II Weyl semimetal surfaces: a review. *Adv. Phys. X* 3:1466661
84. Nurit A, Jonathan R, Abhay K-N, Noam M, Rajib B, et al. 2018. Quasiparticle interference studies of quantum materials. *Adv. Mater* 30:1707628
85. Yang S-Y, Yang H, Derunova E, Parkin SSP, Yan B, Ali MN. 2018. Symmetry demanded topological nodal-line materials. *Adv. Phys. X* 3:1414631
86. Xu S-Y, Alidoust N, Belopolski I, Yuan Z, Bian G, et al. 2015. Discovery of a Weyl fermion state with Fermi arcs in niobium arsenide. *Nat. Phys.* 11:748–54
87. Xu N, Weng HM, Lv BQ, Matt CE, Park J, et al. 2015. Observation of Weyl nodes and Fermi arcs in tantalum phosphide. *Nat. Commun.* 7:11006
88. Belopolski I, Xu S-Y, Sanchez DS, Chang G, Guo C, et al. 2016. Criteria for directly detecting topological Fermi arcs in Weyl semimetals. *Phys. Rev. Lett.* 116:066802

89. Liu ZK, Yang LX, Sun Y, Zhang T, Peng H, et al. 2015. Evolution of the Fermi surface of Weyl semimetals in the transition metal pnictide family. *Nat. Mater.* 15:27–31
90. Souma S, Wang Z, Kotaka H, Sato T, Nakayama K, et al. 2016. Direct observation of nonequivalent Fermi-arc states of opposite surfaces in the noncentrosymmetric Weyl semimetal NbP. *Phys. Rev. B* 93:161112
91. Xu S-Y, Belopolski I, Sanchez DS, Zhang C, Chang G, et al. 2015. Experimental discovery of a topological Weyl semimetal state in TaP. *Sci. Adv.* 1:e1501092
92. Xu D-F, Du Y-P, Wang Z, Li Y-P, Niu X-H, et al. 2015. Observation of Fermi arcs in non-centrosymmetric Weyl semi-metal candidate NbP. *Chin. Phys. Lett.* 32:107101
93. Xu Q, Liu E, Shi W, Muechler L, Gayles J, et al. 2018. Topological surface Fermi arcs in the magnetic Weyl semimetal $Co_3Sn_2S_2$. *Phys. Rev. B* 97:235416
94. Wang Q, Xu Y, Lou R, Liu Z, Li M, et al. 2018. Large intrinsic anomalous Hall effect in half-metallic ferromagnet Co_3Sn2S_2 with magnetic Weyl fermions. *Nat. Commun.* 9:3681
95. Belopolski I, Sanchez DS, Chang G, Manna K, Ernst B, et al. 2017. A three-dimensional magnetic topological phase. arXiv:1712.09992 [cond-mat.mtrl-sci]
96. Chang G, Xu S-Y, Zheng H, Singh B, Hsu C-H, et al. 2016. Room-temperature magnetic topological Weyl fermion and nodal line semimetal states in half-metallic Heusler Co_2TiX (X = Si, Ge, or Sn). *Sci. Rep.* 6:38839
97. Wang Z, Vergniory MG, Kushwaha S, Hirschberger M, Chulkov EV, et al. 2016. Time-reversal-breaking Weyl fermions in magnetic Heusler alloys. *Phys. Rev. Lett.* 117:236401
98. Ernst B, Sahoo R, Sun Y, Nayak J, Muechler L, et al. 2017. Manifestation of the Berry curvature in Co_2TiSn Heusler films. arXiv:1710.04393 [cond-mat.mtrl-sci]
99. Kübler J, Felser C. 2016. Weyl points in the ferromagnetic Heusler compound Co_2MnAl. *Europhys. Lett.* 114:47005
100. Nakatsuji S, Kiyohara N, Higo T. 2015. Large anomalous Hall effect in a non-collinear antiferromagnet at room temperature. *Nature* 527:212–15
101. Nayak AK, Fischer JE, Sun Y, Yan B, Karel J, et al. 2016. Large anomalous Hall effect driven by a nonvanishing Berry curvature in the noncolinear antiferromagnet Mn_3Ge. *Sci. Adv.* 2:e1501870
102. Hao Y, Yan S, Yang Z, Wu-Jun S, Stuart SPP, Binghai Y. 2017. Topological Weyl semimetals in the chiral antiferromagnetic materials Mn_3Ge and Mn_3Sn. *New J. Phys.* 19:015008
103. Kuroda K, Tomita T, Suzuki MT, Bareille C, Nugroho AA, et al. 2017. Evidence for magnetic Weyl fermions in a correlated metal. *Nat. Mater.* 16:1090–95
104. Cano J, Bradlyn B, Wang Z, Hirschberger M, Ong NP, Bernevig BA. 2017. Chiral anomaly factory: creating Weyl fermions with a magnetic field. *Phys. Rev. B* 95:161306
105. Xiong J, Kushwaha SK, Liang T, Krizan JW, Hirschberger M, et al. 2015. Evidence for the chiral anomaly in the Dirac semimetal Na_3Bi. *Science* 350:413–16
106. Li C-Z, Wang L-X, Liu H, Wang J, Liao Z-M, Yu D-P. 2015. Giant negative magnetoresistance induced by the chiral anomaly in individual Cd_3As_2 nanowires. *Nat. Commun.* 6:10137
107. Li Q, Kharzeev DE, Zhang C, Huang Y, Pletikosic I, et al. 2016. Chiral magnetic effect in $ZrTe_5$. *Nat. Phys.* 12:550–54
108. Nakajima Y, Hu R, Kirshenbaum K, Hughes A, Syers P, et al. 2015. Topological RPdBi half-Heusler semimetals: a new family of noncentrosymmetric magnetic superconductors. *Sci. Adv.* 1:e1500242
109. Hirschberger M, Kushwaha S, Wang Z, Gibson Q, Liang S, et al. 2016. The chiral anomaly and thermopower of Weyl fermions in the half-Heusler GdPtBi. *Nat. Mater* 15:1161–65
110. Shekhar C, Nayak AK, Singh S, Kumar N, Wu S-C, et al. 2016. Observation of chiral magneto-transport in RPtBi topological Heusler compounds. arXiv:1604.01641 [cond-mat.mtrl-sci]
111. Wu Y, Mou D, Jo NH, Sun K, Huang L, et al. 2016. Observation of Fermi arcs in type-II Weyl semimetal candidate WTe_2. *Phys. Rev. B* 94:121113(R)
112. Wang C, Zhang Y, Huang J, Nie S, Liu G, et al. 2016. Observation of Fermi arc and its connection with bulk states in the candidate type-II Weyl semimetal WTe_2. *Phys. Rev. B* 94:241119
113. Bruno FY, Tamai A, Wu QS, Cucchi I, Barreteau C, et al. 2016. Observation of large topologically trivial Fermi arcs in the candidate type-II Weyl WTe_2. *Phys. Rev. B* 94:121112

114. Wang Z, Gresch D, Soluyanov AA, Xie W, Kushwaha S, et al. 2016. $MoTe_2$: a type-II Weyl topological metal. *Phys. Rev. Lett.* 117:056805
115. Huang L, McCormick TM, Ochi M, Zhao Z, Suzuki M-T, et al. 2016. Spectroscopic evidence for a type II Weyl semimetallic state in $MoTe_2$. *Nat. Mater* 15:1155–60
116. Deng K, Wan G, Deng P, Zhang K, Ding S, et al. 2016. Experimental observation of topological Fermi arcs in type-II Weyl semimetal $MoTe_2$. *Nat. Phys.* 12:1105–10
117. Belopolski I, Sanchez DS, Ishida Y, Pan X, Yu P, et al. 2016. Discovery of a new type of topological Weyl fermion semimetal state in $Mo_xW_{1-x}Te_2$. *Nat. Commun.* 7:13643
118. Belopolski I, Xu S-Y, Ishida Y, Pan X, Yu P, et al. 2016. Fermi arc electronic structure and Chern numbers in the type-II Weyl semimetal candidate $Mo_xW_{1-x}Te_2$. *Phys. Rev. B* 94:085127
119. Jiang J, Liu ZK, Sun Y, Yang HF, Rajamathi CR, et al. 2017. Signature of type-II Weyl semimetal phase in $MoTe_2$. *Nat. Commun.* 8:13973
120. Liang A, Huang J, Nie S, Ding Y, Gao Q, et al. 2016. Electronic evidence for type II Weyl semimetal state in $MoTe_2$. arXiv:1604.01706 [cond-mat.mtrl-sci]
121. Xu N, Wang ZJ, Weber AP, Magrez A, Bugnon P, et al. 2016. Discovery of Weyl semimetal state violating Lorentz invariance in $MoTe_2$. arXiv:1604.02116 [cond-mat.mtrl-sci]
122. Tamai A, Wu QS, Cucchi I, Bruno FY, Riccò S, et al. 2016. Fermi arcs and their topological character in the candidate type-ii Weyl semimetal $MoTe_2$. *Phys. Rev. X* 6:031021
123. Koepernik K, Kasinathan D, Efremov DV, Khim S, Borisenko S, et al. 2016. $TaIrTe_4$: a ternary type-II Weyl semimetal. *Phys. Rev. B* 93:201101
124. Belopolski I, Yu P, Sanchez DS, Ishida Y, Chang T-R, et al. 2017. Signatures of a time-reversal symmetric Weyl semimetal with only four Weyl points. *Nat. Commun.* 8:942
125. Autès G, Gresch D, Troyer M, Soluyanov AA, Yazyev OV. 2016. Robust type-II Weyl semimetal phase in transition metal diphosphides XP_2 (X = Mo, W). *Phys. Rev. Lett.* 117:066402
126. Liu ZK, Zhou B, Zhang Y, Wang ZJ, Weng HM, et al. 2014. Discovery of a three-dimensional topological Dirac semimetal, Na_3Bi. *Science* 343:864–67
127. Neupane M, Xu S-Y, Sankar R, Alidoust N, Bian G, et al. 2014. Observation of a three-dimensional topological Dirac semimetal phase in high-mobility Cd_3As_2. *Nat. Commun.* 5:3786
128. Liu ZK, Jiang J, Zhou B, Wang ZJ, Zhang Y, et al. 2014. A stable three-dimensional topological Dirac semimetal Cd_3As_2. *Nat. Mater* 13:677–81
129. Borisenko S, Gibson Q, Evtushinsky D, Zabolotnyy V, Büchner B, Cava RJ. 2014. Experimental realization of a three-dimensional Dirac semimetal. *Phys. Rev. Lett.* 113:027603
130. Yi H, Wang Z, Chen C, Shi Y, Feng Y, et al. 2014. Evidence of topological surface state in three-dimensional Dirac semimetal Cd_3As_2. *Sci. Rep.* 4:6106
131. Yang B-J, Nagaosa N. 2014. Classification of stable three-dimensional Dirac semimetals with nontrivial topology. *Nat. Commun.* 5:4898
132. Steinberg JA, Young SM, Zaheer S, Kane CL, Mele EJ, Rappe AM. 2014. Bulk Dirac points in distorted spinels. *Phys. Rev. Lett.* 112:036403
133. Watanabe H, Po HC, Vishwanath A, Zaletel M. 2015. Filling constraints for spin-orbit coupled insulators in symmorphic and nonsymmorphic crystals. *PNAS* 112:14551–56
134. Wieder BJ, Kane CL. 2016. Spin-orbit semimetals in the layer groups. *Phys. Rev. B* 94:155108
135. Young SM, Wieder BJ. 2017. Filling-enforced magnetic Dirac semimetals in two dimensions. *Phys. Rev. Lett.* 118:186401
136. Xu S-Y, Xia Y, Wray LA, Jia S, Meier F, et al. 2011. Topological phase transition and texture inversion in a tunable topological insulator. *Science* 332:560–64
137. Brahlek M, Bansal N, Koirala N, Xu S-Y, Neupane M, et al. 2012. Topological-metal to band-insulator transition in $(Bi_{1-x}In_x)_2Se_3$ thin films. *Phys. Rev. Lett.* 109:186403
138. Xu S-Y, Liu C, Alidoust N, Neupane M, Qian D, et al. 2012. Observation of a topological crystalline insulator phase and topological phase transition in $Pb_{1-x}Sn_xTe$. *Nat. Commun.* 3:1192
139. Weng H, Dai X, Fang Z. 2014. Transition-metal pentatelluride $ZrTe_5$ and $HfTe_5$: a paradigm for large-gap quantum spin Hall insulators. *Phys. Rev. X* 4:011002

140. Manzoni G, Gragnaniello L, Autès G, Kuhn T, Sterzi A, et al. 2016. Evidence for a strong topological insulator phase in $ZrTe_5$. *Phys. Rev. Lett.* 117:237601
141. Park J, Lee G, Wolff-Fabris F, Koh YY, Eom MJ, et al. 2011. Anisotropic Dirac fermions in a Bi square net of $SrMnBi_2$. *Phys. Rev. Lett.* 107:126402
142. Feng Y, Wang Z, Chen C, Shi Y, Xie Z, et al. 2014. Strong anisotropy of Dirac cones in $SrMnBi_2$ and $CaMnBi_2$ revealed by angle-resolved photoemission spectroscopy. *Sci. Rep.* 4:5385
143. Liu JY, Hu J, Zhang Q, Graf D, Cao HB, et al. 2017. A magnetic topological semimetal $Sr_{1-y}Mn_{1-z}Sb_2$ $(y, z < 0.10)$. *Nat. Mater* 16:905–10
144. Kargarian M, Randeria M, Lu Y-M. 2016. Are the surface Fermi arcs in Dirac semimetals topologically protected? *PNAS* 113:8648–52
145. Bian G, Chang T-R, Zheng H, Velury S, Xu S-Y, et al. 2016. Drumhead surface states and topological nodal-line fermions in $TlTaSe_2$. *Phys. Rev. B* 93:121113
146. Fang C, Chen Y, Kee H-Y, Fu L. 2015. Topological nodal line semimetals with and without spin-orbital coupling. *Phys. Rev. B* 92:081201
147. Xie LS, Schoop LM, Seibel EM, Gibson QD, Xie W, Cava RJ. 2015. A new form of Ca_3P_2 with a ring of Dirac nodes. *APL Mater*. 3:083602
148. Yu R, Weng H, Fang Z, Dai X, Hu X. 2015. Topological node-line semimetal and Dirac semimetal state in antiperovskite Cu_3PdN. *Phys. Rev. Lett.* 115:036807
149. Kim Y, Wieder BJ, Kane CL, Rappe AM. 2015. Dirac line nodes in inversion-symmetric crystals. *Phys. Rev. Lett.* 115:036806
150. Chiu C-K, Schnyder AP. 2014. Classification of reflection-symmetry-protected topological semimetals and nodal superconductors. *Phys. Rev. B* 90:205136
151. Wu Y, Wang L-L, Mun E, Johnson DD, Mou D, et al. 2016. Dirac node arcs in $PtSn_4$. *Nat. Phys.* 12:667–71
152. Ekahana SA, Shu-Chun W, Juan J, Kenjiro O, Dharmalingam P, et al. 2017. Observation of nodal line in non-symmorphic topological semimetal InBi. *New J. Phys.* 19:065007
153. Feng X, Yue C, Song Z, Wu Q, Wen B. 2018. Topological Dirac nodal-net fermions in AlB_2-type TiB_2 and ZrB_2. *Phys. Rev. Mater* 2:014202
154. Schoop LM, Ali MN, Straszer C, Topp A, Varykhalov A, et al. 2016. Dirac cone protected by non-symmorphic symmetry and three-dimensional Dirac line node in ZrSiS. *Nat. Commun.* 7:11696
155. Neupane M, Belopolski I, Hosen MM, Sanchez DS, Sankar R, et al. 2016. Observation of topological nodal fermion semimetal phase in ZrSiS. *Phys. Rev. B* 93:201104
156. Hu J, Tang Z, Liu J, Liu X, Zhu Y, et al. 2016. Evidence of topological nodal-line fermions in ZrSiSe and ZrSiTe. *Phys. Rev. Lett.* 117:016602
157. Takane D, Wang Z, Souma S, Nakayama K, Trang CX, et al. 2016. Dirac-node arc in the topological line-node semimetal HfSiS. *Phys. Rev. B* 94:121108
158. Chen C, Xu X, Jiang J, Wu SC, Qi YP, et al. 2017. Dirac line nodes and effect of spin-orbit coupling in the nonsymmorphic critical semimetals MSiS ($M =$ Hf, Zr). *Phys. Rev. B* 95:125126
159. Yamakage A, Yamakawa Y, Tanaka Y, Okamoto Y. 2015. Line-node Dirac semimetal and topological insulating phase in noncentrosymmetric pnictides CaAgX ($X =$ P, As). *J. Phys. Soc. Jpn.* 85:013708
160. Wang X-B, Ma X-M, Emmanouilidou E, Shen B, Hsu C-H, et al. 2017. Topological surface electronic states in candidate nodal-line semimetal CaAgAs. *Phys. Rev. B* 96:161112
161. Liang Q-F, Zhou J, Yu R, Wang Z, Weng H. 2016. Node-surface and node-line fermions from nonsymmorphic lattice symmetries. *Phys. Rev. B* 93:085427
162. Bzdušek T, Wu Q, Rüegg A, Sigrist M, Soluyanov AA. 2016. Nodal-chain metals. *Nature* 538:75–78
163. Wang S-S, Liu Y, Yu Z-M, Sheng X-L, Yang SA. 2017. Hourglass Dirac chain metal in rhenium dioxide. *Nat. Commun.* 8:1844
164. Bi R, Yan Z, Lu L, Wang Z. 2017. Nodal-knot semimetals. *Phys. Rev. B* 96:201305
165. Chen W, Lu H-Z, Hou J-M. 2017. Topological semimetals with a double-helix nodal link. *Phys. Rev. B* 96:041102
166. Yan Z, Bi R, Shen H, Lu L, Zhang S-C, Wang Z. 2017. Nodal-link semimetals. *Phys. Rev. B* 96:041103

167. Chang G, Xu S-Y, Zhou X, Huang S-M, Singh B, et al. 2017. Topological Hopf and chain link semimetal states and their application to Co_2MnGa. *Phys. Rev. Lett.* 119:156401
168. Wieder BJ. 2018. Threes company. *Nat. Phys.* 14:329–30
169. Lv BQ, Feng ZL, Xu QN, Gao X, Ma JZ, et al. 2017. Observation of three-component fermions in the topological semimetal molybdenum phosphide. *Nature* 546:627–31
170. Ma JZ, He JB, Xu YF, Lv BQ, Chen D, et al. 2018. Three-component fermions with surface Fermi arcs in tungsten carbide. *Nat. Phys.* 14:349–54
171. Gao W, Hao N, Zheng F-W, Ning W, Wu M, et al. 2017. Extremely large magnetoresistance in a topological semimetal candidate pyrite $PtBi_2$. *Phys. Rev. Lett.* 118:256601
172. Narayanan A, Watson MD, Blake SF, Bruyant N, Drigo L, et al. 2015. Linear magnetoresistance caused by mobility fluctuations in *n*-doped Cd_3As_2. *Phys. Rev. Lett.* 114:117201
173. Wang K, Graf D, Lei H, Tozer SW, Petrovic C. 2011. Quantum transport of two-dimensional Dirac fermions in $SrMnBi_2$. *Phys. Rev. B* 84:220401
174. Novak M, Sasaki S, Segawa K, Ando Y. 2015. Large linear magnetoresistance in the Dirac semimetal TlBiSSe. *Phys. Rev. B* 91:041203
175. Yi-Yan W, Qiao-He Y, Tian-Long X. 2016. Large linear magnetoresistance in a new Dirac material $BaMnBi_2$. *Chin. Phys. B* 25:107503
176. Xiong J, Kushwaha S, Krizan J, Liang T, Cava RJ, Ong NP. 2016. Anomalous conductivity tensor in the Dirac semimetal Na_3Bi. *Europhys. Lett.* 114:27002
177. Masuda H, Sakai H, Tokunaga M, Yamasaki Y, Miyake A, et al. 2016. Quantum Hall effect in a bulk antiferromagnet $EuMnBi_2$ with magnetically confined two-dimensional Dirac fermions. *Sci. Adv.* 2:e1501117
178. He LP, Hong XC, Dong JK, Pan J, Zhang Z, et al. 2014. Quantum transport evidence for the three-dimensional Dirac semimetal phase in Cd_3As_2. *Phys. Rev. Lett.* 113:246402
179. Wang Z, Zheng Y, Shen Z, Lu Y, Fang H, et al. 2016. Helicity-protected ultrahigh mobility Weyl fermions in NbP. *Phys. Rev. B* 93:121112
180. Yang X, Liu Y, Wang Z, Zheng Y, Xu Z-a. 2015. Chiral anomaly induced negative magnetoresistance in topological Weyl semimetal NbAs. arXiv:1506.03190 [cond-mat.mtrl-sci]
181. Zhang C, Guo C, Lu H, Zhang X, Yuan Z, et al. 2015. Large magnetoresistance over an extended temperature regime in monophosphides of tantalum and niobium. *Phys. Rev. B* 92:041203(R)
182. Zhang C-L, Yuan Z, Jiang Q-D, Tong B, Zhang C, et al. 2017. Electron scattering in tantalum monoarsenide. *Phys. Rev. B* 95:085202
183. Huang X, Zhao L, Long Y, Wang P, Chen D, et al. 2015. Observation of the chiral-anomaly-induced negative magnetoresistance in 3D Weyl semimetal TaAs. *Phys. Rev. X* 5:031023
184. Wang YL, Thoutam LR, Xiao ZL, Hu J, Das S, et al. 2015. Origin of the turn-on temperature behavior in WTe_2. *Phys. Rev. B* 92:180402
185. Zhao Y, Liu H, Yan J, An W, Liu J, et al. 2015. Anisotropic magnetotransport and exotic longitudinal linear magnetoresistance in WTe_2 crystals. *Phys. Rev. B* 92:041104
186. Zhu Z, Lin X, Liu J, Fauqué B, Tao Q, et al. 2015. Quantum oscillations, thermoelectric coefficients, and the Fermi surface of semimetallic WTe_2. *Phys. Rev. Lett.* 114:176601
187. Wang A, Graf D, Liu Y, Du Q, Zheng J, et al. 2017. Large magnetoresistance in the type-II Weyl semimetal WP_2. *Phys. Rev. B* 96:121107
188. Wang C-L, Zhang Y, Huang J-W, Liu G-D, Liang A-J, et al. 2017. Evidence of electron-hole imbalance in WTe_2 from high-resolution angle-resolved photoemission spectroscopy. *Chin. Phys. Lett.* 34:097305
189. Thirupathaiah S, Jha R, Pal B, Matias JS, Das PK, et al. 2017. $MoTe_2$: an uncompensated semimetal with extremely large magnetoresistance. *Phys. Rev. B* 95:241105
190. Chamber RG. 1990. *Electrons in Metals and Semiconductors*. New York: Chapman and Hall
191. Luo Y, Ghimire NJ, Wartenbe M, Choi H, Neupane M, et al. 2015. Electron-hole compensation effect between topologically trivial electrons and nontrivial holes in NbAs. *Phys. Rev. B* 92:205134
192. Hu J, Liu JY, Graf D, Radmanesh SMA, Adams DJ, et al. 2016. π Berry phase and Zeeman splitting of Weyl semimetal TaP. *Sci. Rep.* 6:18674

193. Du J, Wang H, Mao Q, Khan R, Xu B, et al. 2016. Large unsaturated positive and negative magnetoresistance in Weyl semimetal TaP. *Sci. China Phys. Mech. Astron.* 59:657406
194. Ghimire NJ, Yongkang L, Neupane M, Williams DJ, Bauer ED, Ronning F. 2015. Magnetotransport of single crystalline NbAs. *J. Phys. Condens. Matter* 27:152201
195. Abrikosov AA. 1998. Quantum magnetoresistance. *Phys. Rev. B* 58:2788–94
196. Datta S. 1995. *Electronic Transport in Mesoscopic Systems*. Cambridge, UK: Cambridge Univ. Press
197. Chen YL, Chu J-H, Analytis JG, Liu ZK, Igarashi K, et al. 2010. Massive Dirac fermion on the surface of a magnetically doped topological insulator. *Science* 329:659–62
198. Beidenkopf H, Roushan P, Seo J, Gorman L, Drozdov I, et al. 2011. Spatial fluctuations of helical Dirac fermions on the surface of topological insulators. *Nat. Phys.* 7:939–43
199. Okada Y, Dhital C, Zhou W, Huemiller ED, Lin H, et al. 2011. Direct observation of broken time-reversal symmetry on the surface of a magnetically doped topological insulator. *Phys. Rev. Lett.* 106:206805
200. Wray LA, Xu S-Y, Xia Y, Hsieh D, Fedorov AV, et al. 2011. A topological insulator surface under strong Coulomb, magnetic and disorder perturbations. *Nat. Phys.* 7:32–37
201. Liu M, Zhang J, Chang C-Z, Zhang Z, Feng X, et al. 2012. Crossover between weak antilocalization and weak localization in a magnetically doped topological insulator. *Phys. Rev. Lett.* 108:036805
202. Ando Y. 2013. Topological insulator materials. *J. Phys. Soc. Jpn.* 82:102001
203. Shoenberg D. 1984. *Magnetic Oscillations in Metals*. Cambridge, UK: Cambridge Univ. Press
204. Kartsovnik MV. 2004. High magnetic fields: a tool for studying electronic properties of layered organic metals. *Chem. Rev.* 104:5737–82
205. McClure JW. 1956. Diamagnetism of graphite. *Phys. Rev.* 104:666–71
206. Ando T. 2008. Physics of graphene: zero-mode anomalies and roles of symmetry. *Prog. Theor. Phys. Suppl.* 176:203–26
207. Berry MV. 1984. Quantal phase factors accompanying adiabatic changes. *Proc. R. Soc. A* 392:45–57
208. Xiao D, Chang M-C, Niu Q. 2010. Berry phase effects on electronic properties. *Rev. Mod. Phys.* 82:1959–2007
209. Mikitik GP, Sharlai YV. 1999. Manifestation of Berry's phase in metal physics. *Phys. Rev. Lett.* 82:2147–50
210. Taskin AA, Ando Y. 2011. Berry phase of nonideal Dirac fermions in topological insulators. *Phys. Rev. B* 84:035301
211. Lv BQ, Xu N, Weng HM, Ma JZ, Richard P, et al. 2015. Observation of Weyl nodes in TaAs. *Nat. Phys.* 11:724–27
212. Lifshitz IM, Kosevich AM. 1956. Theory of magnetic susceptibility in metals at low temperatures. *Sov. Phys. JETP* 2:636–45
213. Kealhofer R, Jang S, Griffin SM, John C, Benavides KA, et al. 2018. Observation of a two-dimensional Fermi surface and Dirac dispersion in $YbMnSb_2$. *Phys. Rev. B* 97:045109
214. Shoenberg D. 1984. Magnetization of a two-dimensional electron gas. *J. Low Temp. Phys.* 56:417–40
215. Champel T, Mineev VP. 2001. de Haas–van Alphen effect in two- and quasi-two-dimensional metals and superconductors. *Philos. Mag. B* 81:55–74
216. Novoselov KS, Geim AK, Morozov SV, Jiang D, Katsnelson MI, et al. 2005. Two-dimensional gas of massless Dirac fermions in graphene. *Nature* 438:197–200
217. Das Sarma S, Stern F. 1985. Single-particle relaxation time versus scattering time in an impure electron gas. *Phys. Rev. B* 32:8442–44
218. Hwang EH, Das Sarma S. 2008. Single-particle relaxation time versus transport scattering time in a two-dimensional graphene layer. *Phys. Rev. B* 77:195412
219. Xiong J, Luo Y, Khoo Y, Jia S, Cava RJ, Ong NP. 2012. High-field Shubnikov–de Haas oscillations in the topological insulator Bi_2Te_2Se. *Phys. Rev. B* 86:045314
220. Pariari A, Dutta P, Mandal P. 2015. Probing the Fermi surface of three-dimensional Dirac semimetal Cd_3As_2 through the de Haas–van Alphen technique. *Phys. Rev. B* 91:155139
221. Hu J, Tang Z, Liu J, Zhu Y, Wei J, Mao Z. 2017. Nearly massless Dirac fermions and strong Zeeman splitting in the nodal-line semimetal ZrSiS probed by de Haas–van Alphen quantum oscillations. *Phys. Rev. B* 96:045127

222. Kumar N, Manna K, Qi Y, Wu S-C, Wang L, et al. 2017. Unusual magnetotransport from Si-square nets in topological semimetal HfSiS. *Phys. Rev. B* 95:121109(R)
223. Jeon S, Zhou BB, Gyenis A, Feldman BE, Kimchi I, et al. 2014. Landau quantization and quasiparticle interference in the three-dimensional Dirac semimetal Cd_3As_2. *Nat. Mater* 13:851–56
224. Moll PJW, Potter AC, Nair NL, Ramshaw BJ, Modic KA, et al. 2016. Magnetic torque anomaly in the quantum limit of Weyl semimetals. *Nat. Commun.* 7:12492
225. Arnold F, Shekhar C, Wu S-C, Sun Y, dos Reis RD, et al. 2016. Negative magnetoresistance without well-defined chirality in the Weyl semimetal TaP. *Nat. Commun.* 7:11615
226. Hu J, Zhu YL, Graf D, Tang ZJ, Liu JY, Mao ZQ. 2017. Quantum oscillation studies of topological semimetal candidate ZrGeM (M = S, Se, Te). *Phys. Rev. B* 95:205134
227. Arnold F, Naumann M, Wu SC, Sun Y, Schmidt M, et al. 2016. Chiral Weyl pockets and Fermi surface topology of the Weyl semimetal TaAs. *Phys. Rev. Lett.* 117:146401
228. Hu J, Zhu Y, Gui X, Graf D, Tang Z, et al. 2018. Quantum oscillation evidence of a topological semimetal phase in ZrSnTe. *Phys. Rev. B* 97:155101
229. Zheng W, Schönemann R, Aryal N, Zhou Q, Rhodes D, et al. 2018. Detailed study of the Fermi surfaces of the type-II Dirac semimetallic candidates $X\mathrm{Te}_2$ (X = Pd, Pt). *Phys. Rev. B* 97:235154
230. Zhu Y, Zhang T, Hu J, Kidd J, Graf D, et al. 2018. Multiple topologically non-trivial bands in non-centrosymmetric YSn_2. *Phys. Rev. B* 98:035117
231. Cai PL, Hu J, He LP, Pan J, Hong XC, et al. 2015. Drastic pressure effect on the extremely large magnetoresistance in WTe_2: quantum oscillation study. *Phys. Rev. Lett.* 115:057202
232. Ali MN, Schoop LM, Garg C, Lippmann JM, Lara E, et al. 2016. Butterfly magnetoresistance, quasi-2D Dirac Fermi surfaces, and a topological phase transition in ZrSiS. *Sci. Adv.* 2:e1601742
233. Singha R, Pariari A, Satpati B, Mandal P. 2017. Large nonsaturating magnetoresistance and signature of nondegenerate Dirac nodes in ZrSiS. *PNAS* 114:2468–73
234. Wang K, Graf D, Wang L, Lei H, Tozer SW, Petrovic C. 2012. Two-dimensional Dirac fermions and quantum magnetoresistance in $CaMnBi_2$. *Phys. Rev. B* 85:041101
235. Li L, Wang K, Graf D, Wang L, Wang A, Petrovic C. 2016. Electron-hole asymmetry, Dirac fermions, and quantum magnetoresistance in $BaMnBi_2$. *Phys. Rev. B* 93:115141
236. Cao J, Liang S, Zhang C, Liu Y, Huang J, et al. 2015. Landau level splitting in Cd_3As_2 under high magnetic fields. *Nat. Commun.* 6:7779
237. Zhao Y, Liu H, Zhang C, Wang H, Wang J, et al. 2015. Anisotropic Fermi surface and quantum limit transport in high mobility three-dimensional Dirac semimetal Cd_3As_2. *Phys. Rev. X* 5:031037
238. Liu J, Hu J, Cao H, Zhu Y, Chuang A, et al. 2016. Nearly massless Dirac fermions hosted by Sb square net in $BaMnSb_2$. *Sci. Rep.* 6:30525
239. Huang S, Kim J, Shelton WA, Plummer EW, Jin R. 2017. Nontrivial Berry phase in magnetic $BaMnSb_2$ semimetal. *PNAS* 114:6256–61
240. Pippard AB. 1965. *The Dynamics of Conduction Electrons*. New York: Gordon and Breach
241. Lv Y-Y, Zhang B-B, Li X, Yao S-H, Chen YB, et al. 2016. Extremely large and significantly anisotropic magnetoresistance in ZrSiS single crystals. *Appl. Phys. Lett.* 108:244101
242. Wang X, Pan X, Gao M, Yu J, Jiang J, et al. 2016. Evidence of both surface and bulk Dirac bands and anisotropic nonsaturating magnetoresistance in ZrSiS. *Adv. Electron. Mater* 2:1600228
243. Zhang C-L, Xu S-Y, Belopolski I, Yuan Z, Lin Z, et al. 2016. Signatures of the Adler–Bell–Jackiw chiral anomaly in a Weyl fermion semimetal. *Nat. Commun.* 7:10735
244. Sankar R, Peramaiyan G, Muthuselvam IP, Butler CJ, Dimitri K, et al. 2017. Crystal growth of Dirac semimetal ZrSiS with high magnetoresistance and mobility. *Sci. Rep.* 7:40603
245. Pezzini S, van Delft MR, Schoop LM, Lotsch BV, Carrington A, et al. 2018. Unconventional mass enhancement around the Dirac nodal loop in ZrSiS. *Nat. Phys.* 14:178–83
246. Fête A, Gariglio S, Berthod C, Li D, Stornaiuolo D, et al. 2014. Large modulation of the Shubnikov–de Haas oscillations by the Rashba interaction at the $LaAlO_3/SrTiO_3$ interface. *New J. Phys.* 16:112002
247. Liu JY, Hu J, Graf D, Zou T, Zhu M, et al. 2017. Unusual interlayer quantum transport behavior caused by the zeroth Landau level in $YbMnBi_2$. *Nat. Commun.* 8:646

248. Fei F, Bo X, Wang R, Wu B, Jiang J, et al. 2017. Nontrivial Berry phase and type-II Dirac transport in the layered material $PdTe_2$. *Phys. Rev. B* 96:041201
249. Wang Q, Guo P-J, Sun S, Li C, Liu K, et al. 2018. Extremely large magnetoresistance and high-density Dirac-like fermions in ZrB_2. *Phys. Rev. B* 97:205105
250. Ran B, Zili F, Xinqi L, Jingjing N, Jingyue W, et al. 2018. Spin zero and large Landé *g*-factor in WTe_2. *New J. Phys.* 20:063026
251. Cohen MH, Falicov LM. 1961. Magnetic breakdown in crystals. *Phys. Rev. Lett.* 7:231–33
252. Matusiak M, Cooper JR, Kaczorowski D. 2017. Thermoelectric quantum oscillations in ZrSiS. *Nat. Commun.* 8:15219
253. Klein O. 1929. Die Reflexion von Elektronen an einem Potentialsprung nach der relativistischen Dynamik von Dirac. *Z. Phys.* 53:157–65
254. Ru-Keng S, Siu GG, Xiu C. 1993. Barrier penetration and Klein paradox. *J. Phys. A Math. Gen.* 26:1001
255. Calogeracos A, Dombey N. 1999. History and physics of the Klein paradox. *Contemp. Phys.* 40:313–21
256. Dombey N, Calogeracos A. 1999. Seventy years of the Klein paradox. *Phys. Rep.* 315:41–58
257. Katsnelson MI, Novoselov KS, Geim AK. 2006. Chiral tunnelling and the Klein paradox in graphene. *Nat. Phys.* 2:620–25
258. Young AF, Kim P. 2009. Quantum interference and Klein tunnelling in graphene heterojunctions. *Nat. Phys.* 5:222–26
259. O'Brien TE, Diez M, Beenakker CWJ. 2016. Magnetic breakdown and Klein tunneling in a type-II Weyl semimetal. *Phys. Rev. Lett.* 116:236401
260. Zhang Y, Bulmash D, Hosur P, Potter AC, Vishwanath A. 2016. Quantum oscillations from generic surface Fermi arcs and bulk chiral modes in Weyl semimetals. *Sci. Rep.* 6:23741
261. Zhang C, Narayan A, Lu S, Zhang J, Zhang H, et al. 2017. Evolution of Weyl orbit and quantum Hall effect in Dirac semimetal Cd_3As_2. *Nat. Commun.* 8:1272
262. Li P, Wen Y, He X, Zhang Q, Xia C, et al. 2017. Evidence for topological type-II Weyl semimetal WTe_2. *Nat. Commun.* 8:2150
263. Zhang Y, Tan Y-W, Stormer HL, Kim P. 2005. Experimental observation of the quantum Hall effect and Berry's phase in graphene. *Nature* 438:201–4
264. Xu Y, Miotkowski I, Liu C, Tian J, Nam H, et al. 2014. Observation of topological surface state quantum Hall effect in an intrinsic three-dimensional topological insulator. *Nat. Phys.* 10:956–63
265. Brüne C, Liu CX, Novik EG, Hankiewicz EM, Buhmann H, et al. 2011. Quantum Hall effect from the topological surface states of strained bulk HgTe. *Phys. Rev. Lett.* 106:126803
266. Büttner B, Liu CX, Tkachov G, Novik EG, Brüne C, et al. 2011. Single valley Dirac fermions in zero-gap HgTe quantum wells. *Nat. Phys.* 7:418–22
267. Uchida M, Nakazawa Y, Nishihaya S, Akiba K, Kriener M, et al. 2017. Quantum Hall states observed in thin films of Dirac semimetal Cd_3As_2. *Nat. Commun.* 8:2274
268. Schumann T, Galletti L, Kealhofer DA, Kim H, Goyal M, Stemmer S. 2018. Observation of the quantum Hall effect in confined films of the three-dimensional Dirac semimetal Cd_3As_2. *Phys. Rev. Lett.* 120:016801
269. Borisenko S, Evtushinsky D, Gibson Q, Yaresko A, Kim T, et al. 2015. Time-reversal symmetry breaking type-II Weyl state in $YbMnBi_2$. arXiv:1507.04847 [cond-mat.mes-hall]
270. Tajima N, Sugawara S, Kato R, Nishio Y, Kajita K. 2009. Effect of the zero-mode Landau level on interlayer magnetoresistance in multilayer massless Dirac fermion systems. *Phys. Rev. Lett.* 102:176403
271. Stormer HL, Tsui DC, Gossard AC. 1999. The fractional quantum Hall effect. *Rev. Mod. Phys.* 71:S298–305
272. Liu Y, Yuan X, Zhang C, Jin Z, Narayan A, et al. 2016. Zeeman splitting and dynamical mass generation in Dirac semimetal $ZrTe_5$. *Nat. Commun.* 7:12516
273. Zhang C-L, Xu S-Y, Wang CM, Lin Z, Du ZZ, et al. 2017. Magnetic-tunnelling-induced Weyl node annihilation in TaP. *Nat. Phys.* 13:979–86
274. Wang H, Liu H, Li Y, Liu Y, Wang J, et al. 2018. Discovery of log-periodic oscillations in ultra-quantum topological materials. *Sci. Adv.* 4:eaau5096

275. Liu H, Jiang H, Wang Z, Joynt R, Xie XC. 2018. Discrete scale invariance in topological semimetals. arXiv:1807.02459 [cond-mat.mtrl-sci]
276. Xu R, Husmann A, Rosenbaum TF, Saboungi ML, Enderby JE, Littlewood PB. 1997. Large magnetoresistance in non-magnetic silver chalcogenides. *Nature* 390:57–60
277. Hu J, Liu TJ, Qian B, Mao ZQ. 2013. Coupling of electronic and magnetic properties in $Fe_{1+y}(Te_{1-x}Se_x)$. *Phys. Rev. B* 88:094505
278. Hu J, Rosenbaum TF. 2008. Classical and quantum routes to linear magnetoresistance. *Nat. Mater* 7:697–700
279. Kuo H-H, Chu J-H, Riggs SC, Yu L, McMahon PL, et al. 2011. Possible origin of the nonmonotonic doping dependence of the in-plane resistivity anisotropy of $Ba(Fe_{1-x}T_x)_2As_2$ (T = Co, Ni, and Cu). *Phys. Rev. B* 84:054540
280. Huynh KK, Tanabe Y, Tanigaki K. 2011. Both electron and hole Dirac cone states in $Ba(FeAs)_2$ confirmed by magnetoresistance. *Phys. Rev. Lett.* 106:217004
281. Wang K, Petrovic C. 2012. Multiband effects and possible Dirac states in $LaAgSb_2$. *Phys. Rev. B* 86:155213
282. Wang K, Graf D, Petrovic C. 2013. Quasi-two-dimensional Dirac fermions and quantum magnetoresistance in $LaAgBi_2$. *Phys. Rev. B* 87:235101
283. Wang A, Zaliznyak I, Ren W, Wu L, Graf D, et al. 2016. Magnetotransport study of Dirac fermions in $YbMnBi_2$ antiferromagnet. *Phys. Rev. B* 94:165161
284. Nagaosa N, Sinova J, Onoda S, MacDonald AH, Ong NP. 2010. Anomalous Hall effect. *Rev. Mod. Phys.* 82:1539–92
285. Smit J. 1955. The spontaneous Hall effect in ferromagnetics. I. *Physica* 21:877–87
286. Berger L. 1970. Side-jump mechanism for the Hall effect of ferromagnets. *Phys. Rev. B* 2:4559–66
287. Onoda M, Nagaosa N. 2002. Topological nature of anomalous Hall effect in ferromagnets. *J. Phys. Soc. Jpn.* 71:19–22
288. Jungwirth T, Niu Q, MacDonald AH. 2002. Anomalous Hall effect in ferromagnetic semiconductors. *Phys. Rev. Lett.* 88:207208
289. Lee W-L, Watauchi S, Miller VL, Cava RJ, Ong NP. 2004. Dissipationless anomalous Hall current in the ferromagnetic spinel $CuCr_2Se_{4-x}Br_x$. *Science* 303:1647–49
290. Husmann A, Singh LJ. 2006. Temperature dependence of the anomalous Hall conductivity in the Heusler alloy Co_2CrAl. *Phys. Rev. B* 73:172417
291. Manyala N, Sidis Y, DiTusa JF, Aeppli G, Young DP, Fisk Z. 2004. Large anomalous Hall effect in a silicon-based magnetic semiconductor. *Nat. Mater* 3:255–62
292. Liu E, Sun Y, Kumar N, Muechler L, Sun A, et al. 2018. Giant anomalous Hall effect in a ferromagnetic kagome-lattice semimetal. *Nat. Phys.* 14:1125–31
293. Barth J, Fecher GH, Balke B, Graf T, Shkabko A, et al. 2011. Anomalous transport properties of the half-metallic ferromagnets Co_2TiSi, Co_2TiGe and Co_2TiSn. *Phil. Trans. R. Soc. A* 369:3588–601
294. Felser C, Hirohata A, eds. 2016. *Heusler Alloys: Properties, Growth, Applications*. Cham, Switz.: Springer Int.
295. Chadov S, Qi X, Kübler J, Fecher GH, Felser C, Zhang SC. 2010. Tunable multifunctional topological insulators in ternary Heusler compounds. *Nat. Mater* 9:541–45
296. Lin H, Wray LA, Xia Y, Xu S, Jia S, et al. 2010. Half-Heusler ternary compounds as new multifunctional experimental platforms for topological quantum phenomena. *Nat. Mater* 9:546–49
297. Al-Sawai W, Lin H, Markiewicz RS, Wray LA, Xia Y, et al. 2010. Topological electronic structure in half-Heusler topological insulators. *Phys. Rev. B* 82:125208
298. Suzuki T, Chisnell R, Devarakonda A, Liu YT, Feng W, et al. 2016. Large anomalous Hall effect in a half-Heusler antiferromagnet. *Nat. Phys.* 12:1119–23
299. Ye L, Kang M, Liu J, von Cube F, Wicker CR, et al. 2018. Massive Dirac fermions in a ferromagnetic kagome metal. *Nature* 555:638–42
300. Pal HK, Maslov DL. 2010. Necessary and sufficient condition for longitudinal magnetoresistance. *Phys. Rev. B* 81:214438

301. Kim H-J, Kim K-S, Wang JF, Sasaki M, Satoh N, et al. 2013. Dirac versus Weyl fermions in topological insulators: Adler-Bell-Jackiw anomaly in transport phenomena. *Phys. Rev. Lett.* 111:246603
302. Wang Y, Liu E, Liu H, Pan Y, Zhang L, et al. 2016. Gate-tunable negative longitudinal magnetoresistance in the predicted type-II Weyl semimetal WTe_2. *Nat. Commun.* 7:13142
303. Lv Y-Y, Li X, Zhang B-B, Deng WY, Yao S-H, et al. 2017. Experimental observation of anisotropic Adler-Bell-Jackiw anomaly in type-II Weyl semimetal $WTe_{1.98}$ crystals at the quasiclassical regime. *Phys. Rev. Lett.* 118:096603
304. Liang S, Lin J, Kushwaha S, Xing J, Ni N, et al. 2018. Experimental tests of the chiral anomaly magnetoresistance in the Dirac-Weyl semimetals Na_3Bi and GdPtBi. *Phys. Rev. X* 8:031002
305. Reis RDd, Ajeesh MO, Kumar N, Arnold F, Shekhar C, et al. 2016. On the search for the chiral anomaly in Weyl semimetals: the negative longitudinal magnetoresistance. *New J. Phys.* 18:085006
306. Udagawa M, Bergholtz EJ. 2016. Field-selective anomaly and chiral mode reversal in type-II Weyl materials. *Phys. Rev. Lett.* 117:086401
307. Yu Z-M, Yao Y, Yang SA. 2016. Predicted unusual magnetoresponse in type-II Weyl semimetals. *Phys. Rev. Lett.* 117:077202
308. Sharma G, Goswami P, Tewari S. 2017. Chiral anomaly and longitudinal magnetotransport in type-II Weyl semimetals. *Phys. Rev. B* 96:045112
309. Burkov AA. 2017. Giant planar Hall effect in topological metals. *Phys. Rev. B* 96:041110
310. Nandy S, Sharma G, Taraphder A, Tewari S. 2017. Chiral anomaly as the origin of the planar Hall effect in Weyl semimetals. *Phys. Rev. Lett.* 119:176804
311. Li P, Zhang CH, Zhang JW, Wen Y, Zhang XX. 2018. Giant planar Hall effect in the Dirac semimetal $ZrTe_{5-\delta}$. *Phys. Rev. B* 98:121108(R)
312. Li H, Wang H-W, He H, Wang J, Shen S-Q. 2018. Giant anisotropic magnetoresistance and planar Hall effect in the Dirac semimetal Cd_3As_2. *Phys. Rev. B* 97:201110
313. Kumar N, Guin SN, Felser C, Shekhar C. 2018. Planar Hall effect in the Weyl semimetal GdPtBi. *Phys. Rev. B* 98:041103
314. Singha R, Roy S, Pariari A, Satpati B, Mandal P. 2018. Planar Hall effect in the type II Dirac semimetal VAl_3. *Phys. Rev. B* 98:081103(R)
315. Wang YJ, Gong JX, Liang DD, Ge M, Wang JR, et al. 2018. Planar Hall effect in type-II Weyl semimetal WTe_2. arXiv:1801.05929 [cond-mat.mtrl-sci]
316. West FG. 1963. Rotating-field technique for galvanomagnetic measurements. *J. Appl. Phys.* 34:1171–73
317. Liang T, Lin J, Gibson Q, Kushwaha S, Liu M, et al. 2018. Anomalous Hall effect in $ZrTe_5$. *Nat. Phys.* 14:451–55
318. Kane CL, Mele EJ. 2005. Z_2 topological order and the quantum spin Hall effect. *Phys. Rev. Lett.* 95:146802
319. Fu L, Kane CL, Mele EJ. 2007. Topological insulators in three dimensions. *Phys. Rev. Lett.* 98:106803
320. Roth A, Brüne C, Buhmann H, Molenkamp LW, Maciejko J, et al. 2009. Nonlocal transport in the quantum spin Hall state. *Science* 325:294–97
321. Kou X, Fan Y, Wang KL. 2017. Review of quantum Hall trio. *J. Phys. Chem. Solids* In press
322. Xu Q, Song Z, Nie S, Weng H, Fang Z, Dai X. 2015. Two-dimensional oxide topological insulator with iron-pnictide superconductor LiFeAs structure. *Phys. Rev. B* 92:205310
323. Wang QH, Kalantar-Zadeh K, Kis A, Coleman JN, Strano MS. 2012. Electronics and optoelectronics of two-dimensional transition metal dichalcogenides. *Nat. Nanotechnol* 7:699–712
324. König M, Wiedmann S, Brüne C, Roth A, Buhmann H, et al. 2007. Quantum spin Hall insulator state in HgTe quantum wells. *Science* 318:766–70
325. Bradlyn B, Elcoro L, Cano J, Vergniory MG, Wang Z, et al. 2017. Topological quantum chemistry. *Nature* 547:298–305
326. Eugene JM. 2015. The winding road to topological insulators. *Phys. Scr.* 2015:014004
327. Wang C, Hughbanks T. 1995. Main group element size and substitution effects on the structural dimensionality of zirconium tellurides of the ZrSiS type. *Inorg. Chem.* 34:5524–29
328. Qi X-L, Hughes TL, Zhang S-C. 2010. Chiral topological superconductor from the quantum Hall state. *Phys. Rev. B* 82:184516

329. Liu X, Wang Z, Xie XC, Yu Y. 2011. Abelian and non-Abelian anyons in integer quantum anomalous Hall effect and topological phase transitions via superconducting proximity effect. *Phys. Rev. B* 83:125105
330. Chang C-Z, Zhang J, Feng X, Shen J, Zhang Z, et al. 2013. Experimental observation of the quantum anomalous Hall effect in a magnetic topological insulator. *Science* 340:167–70
331. Checkelsky JG, Yoshimi R, Tsukazaki A, Takahashi KS, Kozuka Y, et al. 2014. Trajectory of the anomalous Hall effect towards the quantized state in a ferromagnetic topological insulator. *Nat. Phys.* 10:731–36
332. He QL, Pan L, Stern AL, Burks EC, Che X, et al. 2017. Chiral Majorana fermion modes in a quantum anomalous Hall insulator–superconductor structure. *Science* 357:294–99
333. Po HC, Vishwanath A, Watanabe H. 2017. Symmetry-based indicators of band topology in the 230 space groups. *Nat. Commun.* 8:50
334. Tang F, Po HC, Vishwanath A, Wan X. 2019. Comprehensive search for topological materials using symmetry indicators. *Nature* 566:486–89
335. Vergniory MG, Elcoro L, Felser C, Regnault N, Bernevig BA, Wang Z. 2019. A complete catalogue of high-quality topological materials. *Nature* 566:480–85
336. Zhang T, Jiang Y, Song Z, Huang H, He Y, et al. 2019. Catalogue of topological electronic materials. *Nature* 566:475–79
336a. Kruthoff J, de Boer J, Wezel J, Kane CL, Slager R. 2017. Topological classification of crystalline insulators through band structure combinatorics. *Phys. Rev. X* 7:041069
337. Zhou Q, Rhodes D, Zhang QR, Tang S, Schönemann R, Balicas L. 2016. Hall effect within the colossal magnetoresistive semimetallic state of $MoTe_2$. *Phys. Rev. B* 94:121101
338. Rhodes D, Schönemann R, Aryal N, Zhou Q, Zhang QR, et al. 2017. Bulk Fermi surface of the Weyl type-II semimetallic candidate *g*-$MoTe_2$. *Phys. Rev. B* 96:165134
339. Qi Y, Naumov PG, Ali MN, Rajamathi CR, Schnelle W, et al. 2016. Superconductivity in Weyl semimetal candidate $MoTe_2$. *Nat. Commun.* 7:11038
340. Chen FC, Lv HY, Luo X, Lu WJ, Pei QL, et al. 2016. Extremely large magnetoresistance in the type-II Weyl semimetal $MoTe_2$. *Phys. Rev. B* 94:235154
341. Mun E, Ko H, Miller GJ, Samolyuk GD, Bud'ko SL, Canfield PC. 2012. Magnetic field effects on transport properties of $PtSn_4$. *Phys. Rev. B* 85:035135
342. Wang YJ, Liang DD, Ge M, Yang J, Gong JX, et al. 2018. Topological nature of the node-arc semimetal $PtSn_4$ probed by de Haas–van Alphen quantum oscillations. *J. Phys. Condens. Matter* 30:155701
343. Fu C, Scaffidi T, Waissman J, Sun Y, Saha R, et al. 2018. Thermoelectric signatures of the electron-phonon fluid in $PtSn_4$. arXiv:1802.09468 [cond-mat.mtrl-sci]
344. Liang S, Lin J, Kushwaha S, Xing J, Ni N, et al. 2018. Experimental tests of the chiral anomaly magnetoresistance in the Dirac-Weyl semimetals Na_3Bi and GdPtBi. *Phys. Rev. X* 8:031002
345. He JB, Wang DM, Chen GF. 2012. Giant magnetoresistance in layered manganese pnictide $CaMnBi_2$. *Appl. Phys. Lett.* 100:112405
346. He JB, Fu Y, Zhao LX, Liang H, Chen D, et al. 2017. Quasi-two-dimensional massless Dirac fermions in $CaMnSb_2$. *Phys. Rev. B* 95:045128
347. Singha R, Pariari A, Satpati B, Mandal P. 2017. Magnetotransport properties and evidence of a topological insulating state in LaSbTe. *Phys. Rev. B* 96:245138